Review

Activities to Promote the Moon as an Absolute Calibration Reference

Zhenhua Jing [1], Xiuqing Hu [2,3,*], Yang Wang [4], Ronghua Wu [2,3], Lin Chen [2,3], Lu Zhang [2,3], Yu Huang [5], Shuang Wang [6], Shuang Li [1] and Peng Zhang [2,3]

[1]   College of Astronautics, Nanjing University of Aeronautics and Astronautics, Nanjing 211106, China
[2]   Key Laboratory of Radiometric Calibration and Validation for Environmental Satellites, National Satellite Meteorological Center (National Center for Space Weather), China Meteorological Administration, Beijing 100081, China
[3]   Innovation Center for FengYun Meteorological Satellite (FYSIC), Beijing 100081, China
[4]   Key Laboratory of Infrared System Detection and Imaging Technology, Shanghai Institute of Technical Physics, Chinese Academy of Sciences, Shanghai 200083, China
[5]   State Key Laboratory of Applied Optics, Changchun Institute of Optics, Fine Mechanics and Physics, Chinese Academy of Sciences, Changchun 130033, China
[6]   Key Laboratory of Spectral Imaging Technology, Xi'an Institute of Optics and Precision Mechanics, Chinese Academy of Sciences, Xi'an 710119, China
*   Correspondence: huxq@cma.gov.cn

Abstract: The accuracy and consistency of Earth observation (EO) instrument radiometric calibration is a fundamental prerequisite for achieving accurate results and delivering reliable predictions. Frequent calibration and validation (Cal/Val) activities are needed during the instrument's lifetime, and this procedure is often extended to historical archives. Numerous satellites in orbit and proposed future missions have incorporated lunar observation into their vicarious calibration components over recent years, facilitated by the extreme long-term photometric stability of the Moon. Since the birth of the first lunar calibration reference model, lunar-dependent calibration techniques have developed rapidly, and the application and refinement of the lunar radiometric model have become a welcome research focus in the calibration community. Within the context of the development of lunar observation activities and calibration systems globally, we provide a comprehensive review of the activities and results spawned by treating the Moon as a reference for instrument response and categorize them against the understanding of lunar radiometric reference. In general, this appears to be a process of moving from data to instruments, then back into data, working towards a stated goal. Here we highlight lunar radiometric models developed by different institutions or agencies over the last two decades while reporting on the known limitations of these solutions, with unresolved challenges remaining and multiple lunar observation plans and concepts attempting to address them from various perspectives, presenting a temporal development. We also observe that the methods seeking uncertainty reduction at this stage are rather homogeneous, lacking the combination of approaches or results from lunar surface studies conducted by many spacecraft missions, and joint deep learning methods to extract information. The factors that influence the accuracy of the measurement irradiance may be regulated when practical models arrive. As a central element in lunar calibration, the development of an absolute radiometric datum helps to better understand the Earth system.

Keywords: lunar calibration; traceability; space radiometric measurement; Moon; small satellites constellations; remote sensing

1. Introduction

Satellite observations have emerged as an integral part of the information age, delivering a wide range of opportunities for fine-grained quantitative research on multiple

scales and supporting relevant policies and decision-making. In the 60 years since the first satellite was launched [1], multiple satellites from commonly used LEO (low-Earth orbit) and GEO (geosynchronous orbit) platforms have been launched by different national and private space agencies successively. These are equipped with the same or different types and generations of sensors, leaving hundreds of satellites for Earth observation. However, the observation system that they have formed hardly seems to be self-consistent in responding to scientific requirements such as specifying climate change patterns [2], with challenges in instrument calibration being one of the sources. The inability of optical instruments to obtain consistent datasets, especially in reflective solar bands (RSB) [3], has led to continued efforts to capture the true state of the target of interest. Examples of satellites running continuously for decades exist (e.g., Aqua and Terra) [4], while the continuous and high-efficiency operation of satellites beyond their design lifetime remains in doubt. On the other hand, the quantitative capabilities of a single satellite are limited, and the synergistic usage of multi-source data can advantageously complement each other. Recognizing the concerted efforts needed to address the above challenges [5], relevant national agencies and international organizations have initiated projects dedicated to providing absolute accuracy improvement and traceability to SI (International System of Units) standards for multiple instruments from various remote sensing platforms. The Global Space-based Inter-Calibration System (GSICS) [6] and the Working Group on Calibration and Validation (WGCV) [7], as well as its affiliated Infrared Visible Sensors Group (IVOS), represent typical actions currently in place.

Changes in instrument radiometric response are usually attributed to the harsh environment experienced and aging over time. A growing understanding of calibration and feedback from applied products has prompted multiple methods developed across the remote sensing community to aid in instrument health status examination and correction. High-precision SI traceability is challenging to realize with different devices running in space, and the common practice is to trace the scales to stable and recognized pseudo-invariant authoritative sources, such as pseudo-invariant calibration sites [8–10], glacier targets [11–13], and baseline payloads with high calibration accuracy [14,15]. These are methods that provide insight into the instrument. However the reflectance properties of the solar diffuser (SD) in space change over time [16]. In addition, the use of ground-based targets is often influenced by their bidirectional reflectance distribution function (BRDF) behaviors [17] and atmospheric shrouding [18], and other classic scenarios may involve differences in observation geometry and spectral response functions (SRFs) [19,20], making it challenging to significantly minimize SI traceability link uncertainties. The information delivered by these methods can be independent or correlated, and intercomparison and weighted fusion may alleviate the deficiencies present in individual practices [21]. However, the uncertainty inherent in each may still cause the calibrations to show significant variations [22,23]; for example, ASTER-related onboard calibrations have been found to diverge from vicarious calibrations by up to approximately 10% [24]. It might sometimes be beyond us to find a balance in the set of high-confidence results.

A study on the occurrence rate of craters and their radiometric effects revealed that the lunar photometric properties stabilize in the order of 1% over a million years [25], while the Moon is exposed naturally to a homogeneous cold-space background, appearing quite monotonous in color. The excellent nature in which the Moon behaves as a radiation source is well-known, such that the great majority of satellites have the ability to see the brighter Moon against a dark background and receive lunar radiation without traveling via the atmospheric environment. With the intensive study of various pseudo-invariant sources and the development of radiometric calibration techniques, it is widely recognized as a more promising solution for on-orbit optical standards. Furthermore, its potential to reconcile differences in different methods to meet ultimately stringent scientific objectives is also recognized.

Opportunities for Earth-orbiting satellites to see the Moon are not costly; the Moon is sometimes observed by geosynchronous satellites in cold-space corners [26], LEO satellites can

view the Moon periodically by arranging attitude maneuvers [27,28], and flagship satellites usually refrain from frequent large-angle maneuvers, but the Moon can appear unscheduled in the field of view (FOV) of satellites set up with a space-view port [29–31]. Such events can be predicted by spatial relations [32]. As shown in Figure 1, the diversity in the appearance of lunar data stems from differences in sampling mechanisms, which potentially increases the difficulty of extracting lunar radiation and explicitly affects the accuracy with which it reflects instrument characteristics as well as indicates lunar properties. Moreover, there is no guidance documented regarding the issues presently. Despite these disadvantages, instrument operators have shown increasing interest in lunar calibration for monitoring the temporal stability of their instruments over the last two decades [33]. It has gradually emerged as the preferred target for radiometric calibration of satellite sensors, with proposed satellites broadly incorporating lunar observation into their on-orbit missions, especially small satellites that are not equipped with calibration sources [34–36].
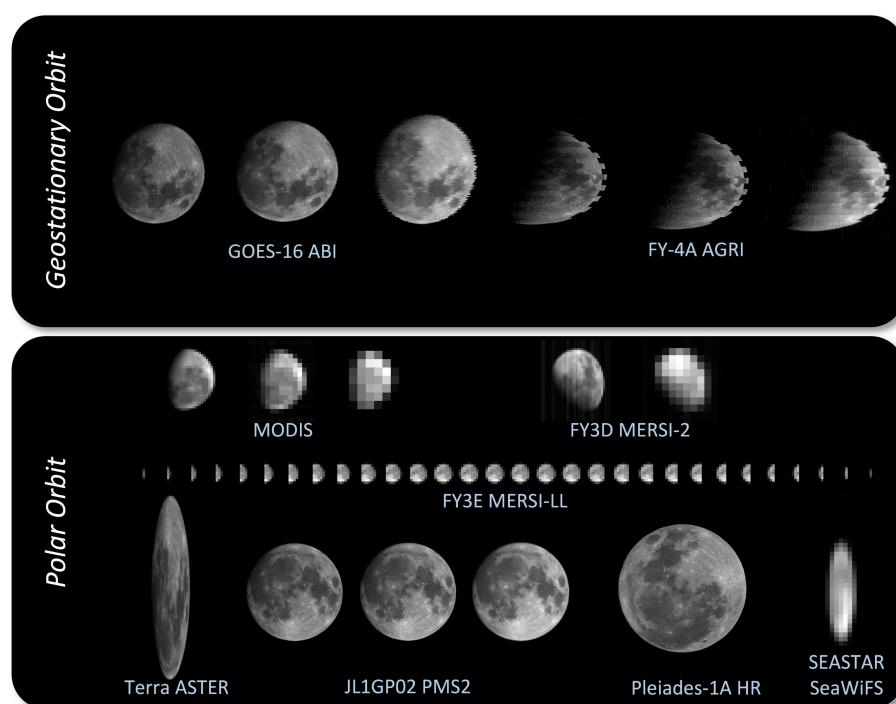

Figure 1. Examples of lunar observations from geostationary and polar-orbiting platforms showing multiple resolutions of the same instrument and illustrating the variety of sampling mechanisms (adapted from [37]).

Treating the directional lunar radiation as a gauge poses several challenges, notably in the strong correlation with lunar phases, repeated in each lunation, and also with differences in patterns shown by the libration. Critical issues in lunar calibration involve quantitative models describing the behavior of lunar brightness, which are usually derived from repeated observations of the Moon over several years, obtaining global radiometric signatures of the nearside of the Moon over time and position. It is worth noting that this review excluded studies looking for photometric models of specific regions of the lunar surface, which typically refer to spacecraft missions. Moreover, even if lunar surface details could be identified (e.g., the geostationary satellites and Pleiades, JL1GP02 satellite listed in Figure 1), such a scheme would provide little help for coarse-resolution data. Several measurement campaigns have been conducted at various sites around the globe; a few have successfully produced a model as an observation geometry with sufficient relative precision. Furthermore, lunar calibration has played a continuing role for nearly two decades. This paper provides a comprehensive review of the developments dedicated to exploiting the Moon as an absolute reference and presents a brief division of the stages along its principal

lines. Figure 2 briefly summarizes the development of the lunar radiometric model and the accompanying and derived measurement activities and mission concepts over the last two decades, which can be coarsely divided into three phases. The first phase began from the ROLO model [38], a pioneering effort to derive multi-year observations into a practical model for describing lunar radiometric behavior, allowing predictions of lunar irradiance for particular observational conditions. This was followed by Miller et al. [39], who developed an irradiance model dedicated to nighttime remote sensing by collecting results from lunar-related multi-source studies. Kouyama et al. developed a disk-resolved radiance-based model with lunar orbiter data [40,41]. The second phase was characterized primarily by implementing high-precision lunar measurement activities dedicated to the critical requirements for absolute lunar reference, a positive response drawing on the lessons learned from several models. The third phase focused on on-orbit SI-traceable lunar observations with the enhanced instruments of the radiometric reference mission. These extensive events were intended facilitate the gathering of comprehensive lunar datasets to anchor the calibration reference to levels of uncertainty below 1%.
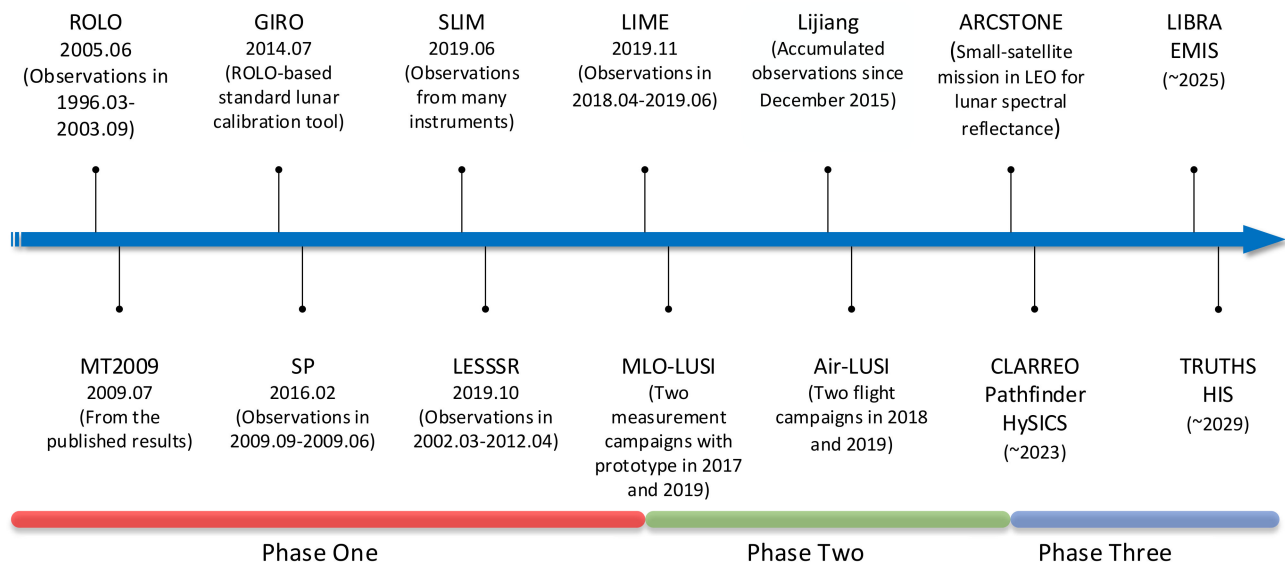

Figure 2. Brief summary of lunar irradiance models and lunar observation campaigns along with mission concepts.

This paper reviewed the above issues in six parts, the first describing the need to develop an absolute lunar radiometric reference. Section 2 starts with the first comprehensive lunar radiometric campaign and describes typical radiometric observation to advance the Moon as a reliable reference and the development of lunar models associated with it. Section 3 describes the projects undertaken to obtain high-precision absolute lunar measurements. Section 4 presents the concept of future SI-traceable satellite instruments for lunar viewing. Section 5 outlines some fundamental issues in the data and model layers, and Section 6 concludes the paper.

2. Lunar Models in Radiometric Calibration

The lunar calibration reference is mainly developed in the form of the equivalent reflectance of the entire lunar disk, but the product tied to the instrument radiometric response for present purposes is the lunar spectral irradiance. This is a practical solution to serve the variety of optical properties of Earth-orbiting spacecraft. Several institutions have constructed such lunar models, and some of the published models' base data properties are summarized in Table 1; Table 2 further lists the geometric constants and some terms important for deriving the lunar irradiance.

Table 1. Summary of lunar radiometric model observations from single data sources.

Model	ROLO	SP	LIME	LESSSR
Instrument	ROLO telescope	SELENE SP	CE318-TP9	Envisat SCIAMACHY
Duration	VNIR: March 1996–September 2003 SWIR: January 1998–September 2003	14 September 2007–10 June 2009	April 2018–October 2020	1 March 2002–8 April 2012
Orbit/Site	USGS Flagstaff Field Center	Lunar polar orbit (No sun-synchronous orbit)	Teide Peak Observatory, Izaña Observatory	Polar orbit
Altitude	2148 m	~100 km	3555, 2401 m	~799 km
FOV	35′	0.23°	1.3°	$1.833 \times 0.0458°$
No. of bands	VNIR: 23; SWIR: 9	296	9	—
Wavelength	VNIR: 350–945 nm SWIR: 945–2500 nm	VIS: 520–960 nm NIR1: 900–1700 nm NIR2: 1007–2600 nm	340–1640 nm	240–2380 nm
Spectral resolution	—	6–8 nm	—	0.24–1.48 nm
Total observations	$>1.1 \times 10^5$ ($>10^6$ star images)	~7000 orbits	~300	~1133

Table 2. Parameters involved in the calculation of the lunar spectral irradiance. (Adapted from [39].)

	Symbol	Description	Value
Distance	$\overline{d}_{Sun-Earth}$	Mean Sun–Earth distance	149,598,022.6 km
	$\overline{d}_{Moon-Earth}$	Mean Moon–Earth distance	384,400 km
	r_{Earth}	Earth radius (equatorial)	6378.14 km
	r_{Moon}	Moon radius	1737.4 km
	AU	Astronomical unit	149,597,870.7 km
	$d_{Viewer-Moon}$	Observer–Moon distance	—
	$d_{Sun-Moon}$	Sun–Moon distance in AU	—
	$d_{Moon-Earth}$	Moon–Earth distance	—
Angle	Ω_{Moon}	Solid angle of the Moon	6.41775×10^{-5}
	Ω_{pixel}	Solid angle of the individual pixel	—
	i	Incidence angle	—
	e	Emission angle	—
	g	Phase angle	—
	θ, φ	Selenographic longitude and latitude of the observer	—
	Φ, Θ	Selenographic longitude and latitude of the Sun	—

In this section, we first summed up a general flow of the lunar radiometric model reference constructed for instrument calibration. For the moment, this is derived from many years of high-precision observations of the Moon, possibly embedded with some empirical or physical representation of photometric knowledge. We then reviewed the first phase of the work listed in Figure 2, the development of models involving the Moon as a calibration reference, presenting the formulation strategies for such models more deeply. Their performance and applications are given in Section 2.9.

2.1. General Form

In general, lunar data collected in terrestrial space from ground to Earth orbit, together with lunar orbit, are available to characterize the instrument's response to itself and serve as a dataset to describe the lunar brightness properties. Only partial results are close to the true lunar radiation, while data recorded by satellites on-orbit are usually applied to indicate the true state of instruments, the former tending to form part of the periodic lunar wax and wane. Enough measurements can be taken to predict the lunar illumination, with the workflow shown in Figure 3. Both states can be formulated abstractly as follows:

$$
\begin{aligned}
E_1 &= f_{\text{meas}}(f(x, y)) \\
E_2 &= f_{\text{model}}(\lambda, t, P_{\text{Observer}}, P_{\text{Moon}}, P_{\text{Sun}})
\end{aligned}
\tag{1}
$$

where $f(x, y)$ denotes the observed lunar image, E_1 is the radiometric value retrieved from it, and E_2 corresponds to E_1 and is typically produced by the multi-parameter function. The observation time t, wavelength λ, and positions P of the observer, Moon, and Sun are a set of prototype parameters.
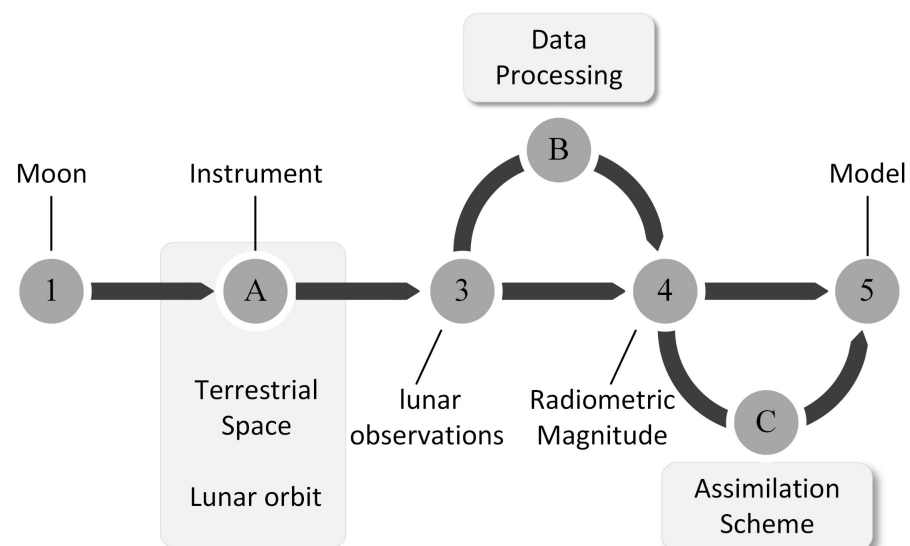

Figure 3. General workflow for formulating lunar reference model.

When describing the lunar brightness, it is usually from E_1 to E_2, while for lunar calibration, E_1 is often adjusted according to the definition of E_2. The most widely adopted method involves integrating radiometric signatures from the nearside of the Moon to the scalar value. The following section details the various lunar calibration references developed, which can all be written as the above formulation.

2.2. Early Lunar Observations

Comprehensive ground-based lunar radiometry was carried out by Lane and Irvine as part of the Brighter Planets Photometry Program, collecting 33 valid observations covering 9 narrower bands (359–1064 nm) and UBV; this was carried out over 29 nights from July 1964 to November 1965 at Le Houga Observatory in southern France [42,43]. The atmospheric extinction coefficients in each band were determined from standard stars observed at different air masses. Following the atmospheric extinction theory of King [44], a detailed atmospheric extinction correction procedure was performed after rejecting observations with exceptionally large extinction residuals and air masses ($\geq$3.5) [43], and all results were corrected to the astronomical unit (AU) and mean Moon–Earth distance.

All lunar magnitudes were fitted as a function of the lunar phase angle, with a combination of linear phase angles smaller than 40° and larger-angle cubic relations

as phase curves. The standard deviation of the fit residuals was typically at 0.05. These results constituted the first integrated data for lunar phase curves in the visible region and also the most comprehensive database before the ground-based lunar observation project described next.

As the astronomical magnitude near the full Moon comes from extrapolation of the linear curve, their study did not account for libration and opposition effects (a sharp surge in the apparent lunar brightness as the phase angle approaches zero phase, usually thought to be shadow-hiding, coherent backscatter, or some combination of the two phenomena) [45,46]. The work represented a major step forward over previous photometric studies that were restricted to particular regions of the Moon [47] or a few wavelengths [48,49], citing almost all preceding related work in their paper and providing a detailed analysis and review. Although the data obtained were insufficient to support high-precision radiometric models, this landmark study greatly motivated subsequent observations and studies to understand lunar disk photometric knowledge.

2.3. First Lunar Irradiance Model

Funded by NASA, the USGS operates a highly automated ROLO program consisting primarily of two telescopes at the Flagstaff Field Center to acquire lunar and stellar images in the visible near-infrared (VNIR) and short-wave infrared (SWIR) ranges. A summary of the ROLO observation is presented in Table 1. The Moon is sampled at approximately 30° above the horizon at approximately 30 min intervals, weather permitting. Stellar observations are not time-limited but are adapted to their intensity by a pair of removable neutral density filters and observed through a fused silica compensator; data acquisition and archiving are carried out under the control of four computers [50]. A database of more than 110,000 lunar images and over 10^6 star images was generated in 7.5 years.

The stellar observations were used to characterize the atmospheric transport properties, processed to irradiance, correlated with exo-atmospheric star magnitudes. Langley analysis was performed on all measurements in the 32 ROLO bands to obtain atmospheric extinction measurements, resulting in a parametric expression describing the atmospheric transmittance over the site as a function of time; this is used for atmospheric correction at the moment of lunar acquisition [51]. On the other hand, the spectral model of Vega was scaled to an absolute reference [52,53] with an average resolution of 0.5 nm [54], referring to the method described in [52]. This, in turn, yields an absolute flux specific to the ROLO band, and the comparison with external atmospheric Vega observations is the starting point for calibrating the ROLO lunar images. The ratios of the neutral density filter and the stellar observation compensator were derived from regular observations of bright stars containing Vega and were eventually used for radiometric calibration. Additionally, they implemented the lamp–plaque calibration system (1000 W standard lamp and Spectralon plaque) for ROLO, but the results changed noticeably over time and showed a large difference of 36% (VNIR) from the stellar-based calibrations [55].

The lunar equivalent disk is obtained from the corrected dataset, and then the spatial integration of radiance images representing the lunar signal, and the image pixel solid angle ultimately yields the irradiance measurements:

$$E_{k,\text{Moon}} = \Omega_{\text{pixel}} \frac{1}{f_{\text{os}}} \sum_{i}^{row} \sum_{j}^{col} L_{i,j} \tag{2}$$

where $L_{i,j}$ is the net radiance covering all image coordinates (i, j) of the lunar equivalent disk, k indicates the band index (omitted in the later section), and f_{os} is the oversampling factor (no oversampling correction is required for ROLO using the area-array camera, but the correction is more common for satellites).

The measured irradiances are normalized to the standard distance (1 AU Sun–Moon and 384,400 km mean Moon–Earth distance) and then converted to disk-integrated reflectance:

$$A_k = \frac{\pi E_{k,\text{Moon}}}{\Omega_{\text{Moon}} E_{k,\text{Sun}}} f_\text{d}$$

$$f_\text{d} = \left(\frac{d_{\text{Sun}-\text{Moon}}}{1\text{AU}} \right)^2 \left(\frac{d_{\text{Viewer}-\text{Moon}}}{384{,}400 \text{ km}} \right)^2 \tag{3}$$

where distance should correspond to the lunar center sampling.

A geometry-dependent form of the lunar reflectance was determined by combining a priori knowledge of the lunar phase angle, heterogeneous surface, libration, and opposite effects. The model was determined empirically by fitting the observed data in each band several times:

$$\ln A_k = \sum_{i=0}^{3} a_{ik} g^i + \sum_{j=1}^{3} b_{jk} \Phi^{2j-1} + c_1 \theta + c_2 \varphi + c_3 \Phi \theta + c_4 \Phi \varphi$$
$$+ d_{1k} e^{-g/p_1} + d_{2k} e^{-g/p_2} + d_{3k} \cos((g - p_3)/p_4) \tag{4}$$

Equation (4) as a function of the absolute lunar phase angle g (radian), the seleno-graphic sub-observer longitude θ, and latitude φ (degree), as well as sub-solar longitude Φ (radian), contains 10 wavelength-dependent coefficients (a, b and d) and 8 constants (c and p), for a total of 328 model coefficients (Table 4 in [38]). The initial fit retained over 1200 observations for each ROLO band for determining the parameters of the empirical model, with mean absolute residuals of less than 1% for each band fitted.

The calibration of the channel-type ROLO instrument relies on the star Vega. The resulting model yields lunar spectra with apparent inter-band deviations that are not in agreement with spectra that are smooth with only broad and shallow absorption features [56] nor with the returned Apollo samples laboratory spectra [57]. This is probably owing to the different path lengths introduced by the variation in zenith angle between the standard stars and the Moon [58].

An adjustment strategy for smoothing 32 ROLO band lunar spectra for particular observing conditions (7° phase angle and selenographic sub-solar longitude, zero libration) is proposed via a certain proportion of Apollo laboratory spectra (lunar soil samples mixed with 5% breccia [57,59]). This was executed by fitting the ratio of ROLO reflectance to the reference spectrum as a linear function of wavelength. The fitted resulting hyperspectral reflectance is convolved with the sensor spectral response function and the solar spectral irradiance to produce a spectral band ROLO reference lunar irradiance specific to the standard observational conditions of the sensor, and thus to obtain a relationship with the observed irradiance:

$$E_{\text{ROLO}} = \frac{\Omega_{\text{Moon}}}{\pi} \frac{\int E_{k,\text{Sun}}(\lambda) A_{k,\text{ROLO}}(\lambda) R_k(\lambda) d\lambda}{\int R_k(\lambda) d\lambda} \tag{5}$$

ROLO, as the initial calibration reference, provides a new approach to calibration for agencies with instruments capable of observing the Moon. As the USGS ROLO model is not yet publicly available, some agencies have developed their individual version from the prototype algorithm. However, discrepancies exist between some implementations and the results of the USGS ROLO model [37]. Several national agencies have extended the practicality of the ROLO model by establishing a limited publicly accessible lunar calibration reference GIRO (GSICS implementation of the ROLO model) with GSICS support. Perturbation simulation tests demonstrated agreement with the ROLO prototype, such as for MSG SEVIRI VIS06, with 377 results showing near-zero percentage differences [60], traceable to ROLO [37,61]. GSICS GIRO has evolved into an internationally accepted standard lunar calibration reference tool. It provides lunar reference irradiance in the wavelength and phase angle range of 350–2500 nm and 2–92°, requiring user-defined observation and sensor spectral response functions in NetCDF format [62]. As the current default

lunar calibration standard, it is distributed to agencies and organizations that include lunar observations in GLOD (GSICS Lunar Observation Dataset, a database with several sets of lunar acquisitions) and circulates only within the GSICS community.

2.4. Lunar Irradiance Based on Early Observations

Motivated by the need for nighttime environmental applications of the VIIRS DNB at natural light scales, Miller and Turner prepared a hyperspectral irradiance model (MT2009) based on published results collected by many researchers over time [39]. The early observations of Lane and Irvine formed the basis of this work, and their derived lunar magnitudes were considered as a given phase angle under a linear function of nine narrow bands. The nonlinear variation in the lunar brightness is therefore described as a phase function in the exponential form:

$$f(\lambda, g) = 10^{-0.4(a(g) - b(g)\lambda)} \tag{6}$$

where a and b are coefficients (Table 3 in [39]).

The curve fitting in two spectral subregions (0.3–0.6 µm and 0.6–1.2 µm), following the geometric albedo data of [63–65], yielded seven coefficients that describe the lunar spectral albedo in the wavelength range of 0.2–1.2 µm:

$$A = \sum_{i=0}^{n} c_i \lambda^i \tag{7}$$

where c_i is the fit coefficient (Table 5 in [39]), and n is the order of fit function for the two spectral regions ($n = 3$, $0.3 < \lambda < 0.6$ µm; $n = 4$, $0.6 \leq \lambda < 1.2$ µm).

Further, assuming that the Moon is a space Lambertian sphere, the equivalent isotropic irradiance from lunar reflection at an arbitrary Sun–Moon distance is obtained using the average solar spectral irradiance as a reference:

$$L_{\text{Moon}} = \frac{E_{\text{Sun}} A}{\pi} \left(\frac{\bar{d}_{\text{Sun−Earth}}}{d_{\text{Sun−Moon}}} \right)^2 \tag{8}$$

The lunar equivalent disk solid angle relative to the Earth can be expressed as:

$$\Omega_{\text{Moon}} = \frac{\pi r_{\text{Moon}}^2}{(d_{\text{Moon−Earth}} - r_{\text{Earth}})^2} \tag{9}$$

The solid angle of the illuminated fraction of the Moon is obtained by taking the phase function as a factor to obtain above-atmosphere lunar irradiance:

$$E_{\text{MT2009}} = L_{\text{Moon}} \Omega_{\text{Moon}} f(\lambda, g) \cos(\theta) \tag{10}$$

where θ is the lunar zenith angle.

Equation (10) defines the irradiance of an observer on Earth and requires an adjustment to the solid angle at an actual position for satellites in orbit. Further, to facilitate operational integration, they define the lookup table version of the irradiance model with standard distances. When the standard lunar irradiance is provided for the average Sun–Moon and Moon–Earth distances, the irradiance at any actual observed location is given by the following equation, and the Sun–Earth distance can further simplify the Sun–Moon distance:

$$E(\lambda) = \frac{\int \bar{E}_{\text{MT2009}}(g, \lambda) R_k(\lambda) d\lambda}{\int R_k(\lambda) d\lambda} F \cos(\theta)$$
$$F = \left(\frac{\bar{d}_{\text{Sun−Earth}}}{d_{\text{Sun−Earth}}} \right)^2 \left(\frac{\bar{d}_{\text{Moon−Earth}} - r_{\text{Earth}}}{d_{\text{Moon−Earth}} - r_{\text{Earth}}} \right)^2 \tag{11}$$

The lookup-table-driven version provides a standard distance lunar irradiance table with 1 nm interval at 1° phase angle resolution, and another table of lunar phase and

Sun–Earth and Earth–Moon distance versus time is integrated. A sensor-specific lunar irradiance table with the same phase angle resolution is generated by convolving the standard table with the SRF, then linearly interpolating it to the actual spatial geometry, and finally scaling by the distance factor and zenith angle items. The lookup table version of the standard model maintains consistency with the full irradiance model to within 0.05% after introducing the distance approximation.

2.5. Hyperspectral Reflectance Model from Lunar Orbital Data

Since the first complete observation of the lunar surface by the U.S. Clementine in 1994 [66], the Japanese lunar orbiter SELENE (SELenological and ENgineering Explorer) [67], the Chinese Chang'e-1 [68], and the Indian Chandrayaan-1 [69] were launched, which enabled many researchers to propose photometric functions and parameters for the Moon. The Japanese SELENE SP (Spectral Profiler) acquired nearly 7000 hyperspectral lunar surface data with 500 m swaths in the nadir direction from 2007 to 2009 at a lunar orbit of approximately 200 km [40,70] (Table 1); furthermore, two additional push-scan imaging payloads (Terrain Camera, TC; Multiband Imager, MI) covered the SP footprint with different swath widths [71].

For radiometric calibration and phase angle coverage constraints, only short-exposure data at wavelengths less than 1645 nm (160 channels) are used to derive photometric correction parameters for the spectral bands on both sides of the Moon. In addition, the calibrated irradiance results are first used to generate the radiance factor (RADF), which is the reflectance relative to a perfectly scattered surface for normal illumination:

$$r_{\text{obs}}(\lambda,\ i,\ e,\ g) = \frac{L_{\text{obs}}(\lambda,\ i,\ e,\ g)}{E_{\text{Sun}}(\lambda)/\pi} \tag{12}$$

where L_{obs} is the observed radiance.

The significance of photometric correction lies in the correction of spectral data from different observation geometries to the standard geometry, and the model can usually be described by two components, the disk function (or limb-darkening function) and the phase function, sometimes introducing a scaling factor to normalize the phase function:

$$r_{\text{SP\_corr}}(\lambda,\ 30°,\ 0°,\ 30°) = r_{\text{obs}}(\lambda,\ i,\ e,\ g)\frac{X_L(30°,\ 0°,\ 30°)}{X_L(i,\ e,\ g)}\frac{f(30°)}{f(g)} \tag{13}$$

where X_L is the linear combination of the high phase angle Lambertian function and the low phase angle Lommel–Seeliger function to represent the disk function, and phase function $f(g)$ is an empirical function for describing the phase angle dependence of the lunar surface reflectance.

The disk function is determined empirically based on [72], and the solution of the phase function parameters relies on the observations performed in different regions due to the SP holding the nadir view. The phase function of McEwen et al. [73] was used as a priori knowledge to produce a reflectance map in 752.8 nm band, which corrected both highland and mare data with an error of less than 1.5% in the 20–40° phase angle region [74].

Considering the inhomogeneous surface of the Moon, a rough geological classification was applied upon the initial reflectance map to obtain three albedo groups (high, medium, and low), and then a simple boundary function was adopted to yield 14, 13, and 18 subgroups of the above albedo groups, respectively, while excluding grid data with coefficients of variation higher than 0.1. The issue of reflectance differences introduced by non-horizontal surfaces is weakened by applying two median filters, and the results from the finer 45 reflectance subgroups were subsequently re-merged into three reflectance groups, where the phase function delivered a clear phase angle dependence. All bands from the three groups were fitted to produce a set of empirical photometric correction parameters, showing that the fit residuals for almost all are below 5% for the 5–75° phase angle and better than 3% for all bands of the high albedo group.

Correlation analysis of the SP data with the other two optical instrument observations was used to identify the highland and mare for checking the consistency of the photometric corrected data. Then, the normalized reflectance for the high and low phase angles was compared with the medium phase angle to obtain the spectral ratios, showing mostly agreement to within 5%. Additionally, they speculated that the differences in average values of spectral ratios for the highland and the results for mare at small phase angles may be affected by topography, and for the mare with large phase angles, they had no plausible explanation for the complex pattern of spectral ratios.

For a solar incidence angle higher than 75°, they found that a clear phase dependence remained between the ratio of the observed RADF to the disk function and the fitted phase function and attributed it to the effect of roughness. This was then further corrected with an additional third-order polynomial as a function of the incidence angle:

$$S(\eta) = 1.0 + s_1\eta + s_2\eta^2 + s_3\eta^3$$
$$r_{\text{SP\_corr}}(\lambda,\ 30°,\ 0°,\ 30°) = r_{\text{SP\_corr}}(\lambda,\ 30°,\ 0°,\ 30°)\frac{1}{S(\eta)} \tag{14}$$

where $\eta = i - 75°$ ($75° < i < 85°$), and s is the coefficient.

The result of the photometric correction is a set of photometric correction parameters in the 500–1600 nm wavelength region, and the product is a global lunar reflectance map cube with 160 spectral bands and 1° resolution in latitude and longitude. The inverse operation of the photometric correction was considered:

$$r_{\text{SP}}(\lambda,\ i,\ e,\ g) = r_{\text{SP\_corr}}(\lambda,\ 30°,\ 0°,\ 30°)\frac{X_L(\lambda,\ i,\ e,\ g)}{X_L(\lambda,\ 30°,\ 0°,\ 30°)}\frac{f(\lambda,\ g)}{f(\lambda,\ 30°)} \tag{15}$$

The SP model is developed essentially in the form of reflectance, and in introducing the solar irradiance model, it allows a disk-resolved radiance-based model to be obtained:

$$R_{\text{SP}}(\lambda,\ 30°,\ 0°,\ 30°) = r_{\text{SP}}(\lambda,\ 30°,\ 0°,\ 30°)\frac{E_{\text{Sun}}(\lambda)}{\pi}\left(\frac{d_{\text{Sun-Moon}}}{1\text{AU}}\right)^2 \tag{16}$$

A basis for intercomparison with the observed image stems from the ability of the SP cube to simulate it, which requires consideration of reprojection and distortion of observed images. The result is a simulated image of the lunar radiance at the sensor's view. After sensor SRF adjustment, the disk-integrated signal allows a radiometric calibration reference for the instrument:

$$E_{\text{SP},k} = \sum_{i=0}^{n} R_{\text{SP},i}(\lambda)\Omega_{\text{pixel},k} \tag{17}$$

In addition, the absolute scale of the SP is corrected by the ROLO model, and since their 16-year average irradiance ratio is almost negatively correlated with wavelength (ratio = ROLO/SP), longer wavelengths indicate slightly higher SP irradiance than the ROLO simulation (Figure 8 in [41]):

$$p(\lambda) = a_0 + a_1\lambda + a_2\lambda^2 + a_3\lambda^3$$
$$r_{\text{SP}}(\lambda,\ i,\ e,\ g) = r_{\text{SP}}(\lambda,\ i,\ e,\ g)p(\lambda) \tag{18}$$

2.6. Irradiance Modeling with Integrated Multi-Source Data

Many lunar spectral data have been recorded from near-Earth space as well as lunar orbit up to now, each with its characteristics in spectral, spatial, and temporal phase coverage. However, none of them have agreed on radiometric calibration. Kieffer integrated observations from some of them, including three ground-based and nine LEO instruments, together with Clementine full lunar spectral reflectance maps, to propose a lunar irradiance model SLIM (spectral lunar irradiance model) [75–79]. This is the first result obtained

by fusing a large number of data, and the SLIM actually provides a method to integrate multi-source lunar spectral irradiance data.

Lunar irradiance measurements at specific times and positions form the basis of SLIM and include observations of broad phase angles (e.g., Pleiades 1A/1B HR), symmetric phase angles (e.g., SeaWiFS, MODIS, and OLI), and several surface observation project datasets (e.g., ROLO, NIST surface observations), along with higher GEO sources (e.g., GOES 16/17 ABI). Integrating these data into the irradiance database derives from the authors' choice of available instruments and the uncertainty assigned to the observations, with only instruments excluding GEO used for model derivation. The irradiance library of approximately 90,000 lunar images from 12 instruments yields a purely data-driven model form. Specifically, the observed lunar radiation is decomposed into the solar irradiance spectrum and lunar equivalent disk reflectance; the latter is expressed further by the lunar reference spectrum and two continuous functions of wavelength and angle derived from the observer–Moon–Sun position:

$$E_{\text{SLIM}}(\lambda) = E_{\text{Sun}}(\lambda) A_{\text{Apollo}}(P_0, \lambda) L(P, \lambda) B(P, \lambda) \frac{\Omega_{\text{Moon}}}{\pi} f_d \qquad (19)$$

where E_{Sun} is treated as variable in SLIM and varies with time and wavelength, A_{Apollo} is the Apollo reference spectrum used for ROLO, and the P here is different from the photometric function defined in [75], but a more basic variable in (1).

The libration model form and coefficients are based on the total lunar reflectance map of spacecraft orbiting the Moon, and the irradiance summed from the resulting orthographic projection map of the instrument's viewpoint is estimated independently as the dependent variable. The included gain term is iteratively estimated for all instruments starting from 1, and the final result is the average over the period covering all observations of the instrument. Thus, the resulting SLIM libration model consists of a combination of corresponding terms containing 24 coefficients and another continuous function involving 34 coefficients, all wavelength independent. Both the total solar irradiance and the spectral variation are also modeled explicitly together, with the recent TSIS-1 hybrid solar reference spectrum (HSRS) used as a reference [80], and the ROLO dataset is updated with the new version of ROLOH accordingly, while the differences introduced by them are not significant.

SLIM is capable of modifying the uncertainty, choice of instruments, and integration or not of the libration model to generate irradiance models of different forms and parameters. The author describes SLIM as having a library of many instruments and a model generation system with many parameters. In addition, when long-term degradation of different instruments is considered, the lunar calibration gains derived from the above model can generate gain-adjusted observed irradiance and reintegrate it into a new model over time. With the addition of improved ROLOH, the model currently named V1 represents the latest version closest to the lunar brightness.

2.7. Improved Irradiance Model Using CE318 Data

Inspired by the ROLO model, an ESA-sponsored multi-agency collaboration carried out ground-based lunar observation experiments traceable to SI at Teide Peak and the Izaña Observatory (the Spanish site of the global Automated Aerosol Observation Network (AERONET), a station with stable atmospheric conditions and exceptionally low aerosol levels) [81]. That was achieved by deploying the CIMEL CE318-TP9 photometer on site, equipped with nine standard channels and three polarized channels. Its predecessor CE318-T was widely used as the master instrument in AERONET. It was reported by Barreto et al. [82] that the lunar measurement mode of the sun–sky–lunar CIMEL CE318-T photometer can obtain extra-atmospheric lunar irradiance with sufficient accuracy.

Since March 2018, the instrument has been sampling the Moon at a frequency of 3 min, with a set of dedicated procedures and near-real-time monitoring to ensure quality and including maintenance rules for regular cleaning and instrument status checks. It is worth noting that a low signal-to-noise ratio (340 and 380 nm) and strong water vapor absorption

channel (940 nm) lunar measurements were ruled out. Unlike the ROLO observations, the CE318-TP9 ground-based project aims for SI-traceable measurements. It includes an assessment of the thermal sensitivity of the instrument, and the linearity and responsivity over the wide dynamic range required for the three observations (called triplet), along with the resulting uncertainties; for example, two independent temperature characterization experiments performed in December 2017 and January 2018, confirming that the 1020 nm channel is most sensitive to temperature. While the lunar photometer is traceable to a cryogenic radiometer standard from the National Physical Laboratory (NPL) in the UK, the lunar gain coefficients can be obtained by up to four calibration methods for each band, considering the gain ratio of the triplet, resulting in a weighted combination. Further, the potential response drift is included. The final extra-atmospheric lunar irradiance is derived from the nighttime Langley fitting procedure, and more details are given by [58]:

$$A = \frac{V_{\text{TOA}}^{\text{Moon}}(\lambda, t)C(\lambda)\pi}{\Omega_{\text{Moon}}E_{\text{Sun}}(\lambda)} \tag{20}$$

where $V_{\text{TOA}}^{\text{Moon}}(\lambda, t)$ is the photometric voltage signal above the atmosphere.

CE318-TP9 obtained a new set of measurements, and the data were integrated in a form referring to the derived equation of the USGS ROLO model, but with minor modifications. They define independent c-coefficients for the lunar libration dependence terms, which are spectrally independent in the ROLO model, are as follows:

$$\ln A_k = \sum_{i=0}^{3} a_{ik}g^i + \sum_{j=1}^{3} b_{jk}\Phi^{2j-1} + c_{1k}\theta + c_{2k}\varphi + c_{3k}\Phi\theta + c_{4k}\Phi\varphi \\ + d_{1k}e^{-g/p_1} + d_{2k}e^{-g/p_2} + d_{3k}\cos((g - p_3)/p_4) \tag{21}$$

The model coefficients are fitted sequentially from the linear and nonlinear components. Each band has one set of linear and nonlinear parameters, forming six group model parameters for the six bands in addition to the p parameter. Additionally, the CE381-TP photometer allows multi-angle polarization measurements of the Moon, while previous studies have found that moonlight is linearly polarized and usually follows the Umov effect [83–85]. On the basis of directly measuring the degree of linear polarization (DoLP), simplified polarimetric models describing the polarimetric characteristics of the Moon under waxing and waning Moon conditions were formulated. They are expressed as fourth-order polynomials with intercept 0:

$$P_{\text{DoLp}} = a_1 g + a_2 g^2 + a_3 g^3 + a_4 g^4 \tag{22}$$

They also found that DoLP is spectrally dependent, increasing with phase angle. Furthermore, LIME (Lunar Irradiance Model ESA) coefficients incorporating polarization are available at https://calvalportal.ceos.org/lime (accessed on 12 September 2021). Important to note is that their model will be re-evaluated against the latest continuously joined measurements.

2.8. Lunar Irradiance Model with Space-Based Data

Ground-based instrument measurements with repeatable high-precision calibrations are the preferred choice for quantifying lunar radiation, while on-orbit observations can also serve as a characteristic dataset for quantifying lunar brightness. SCIAMACHY operated as an atmospheric science instrument on-board the European Environmental Satellite (ENVISAT) between 2002 and 2012. It provided continuous spectra from 240 to 2380 nm over 8 channels and also 7 polarization channels, with sophisticated design and multiple observation modes [86,87]. As one of the stable sources, 1133 lunar measurements were recorded, and dense sampling was performed for 6 months. In lunar observation mode, light is passed in the scanning mirror system from the ASM (azimuth scan module) mirror to the ESM (elevation scan module) reflector and then to the optical bench module (OBM);

studies have shown degradation in both ASM and ESM [88]. SCIAMACHY Level 1 data have been updated several times in response to radiometric calibration issues. The newly evolved SCIAMACHY hyperspectral lunar data constitute a comparatively well-developed database of measurements with a state ID of 54, indicating a complete lunar scan. They are stored in the SCIAMACHY archive, representing the standard processed lunar reflectance.

Differences were found initially between SCIAMACHY-based and laboratory-based reflectance of Apollo samples and the GIRO model, such as shallower spectral absorption features around 1000 nm. It was considered that they were mainly related to elements such as scanner contamination, polarization sensitivity, and BRDF correction from the diffuser [89]. Studies of the SCIAMACHY solar spectrum have motivated recalibration and yielded an improved lunar dataset [90,91]. However, inadequate polarization measurements by on-board polarization measurement devices and the scan angle dependence of ASM and ESM mirror degradation causing observed reflectance continues to involve systematic errors:

$$\ln A_{\text{meas}} = \ln A_{\text{model}} + f_{\text{inst}} \tag{23}$$

where A_{meas} is the SCIAMACHY measured reflectance, A_{model} is the reflectance with systematic errors removed, and f_{inst} is a function describing the systematic errors.

The analytical form of the observation geometry components is partly founded on the ROLO model, with minimally fitting residuals driving the possible higher order and cross-term dependence tests for these terms, which ultimately holds them at lower order levels. The brightness behavior for small phase angles is fixed, employing two exponential terms analogous to the ROLO model. The residual is a cosine function of the phase angle, resulting in the following equation:

$$\begin{aligned}
\ln A_{\text{ref}} = {} & p_0 + p_1 g^{1/2} + p_2 g + p_1 g^{3/2} + p_4 \Phi + p_5 \varphi + p_6 \theta + p_7 e^{-g p_8} \\
& + p_9 e^{-g p_{10}} + p_{11} \cos((g - p_{12})/p_{13})
\end{aligned} \tag{24}$$

where p is the coefficient, and the rest of the letters refer to the ROLO model.

The revised SCIAMACHY lunar reflectance dataset was fitted independently to each wavelength using Equation (24) and followed a strict order regression parameter, with the final residuals fitted to the polarization function [92]. Additionally, SCIAMACHY lunar reflectance is compromised by bad detectors and intrinsic noise detectors at wavelengths beyond 1600 nm, and the resulting reflectance is supplemented by RELAB reflectance (300–2600 nm) determined in standard geometry. A total of 80 reference spectra were selected for various lunar soil materials, and the optimal linear combination of such spectra was fitted to the derived reflectance and again fitted as a function of the observation geometry to spectra at 5 nm intervals, thus extending the spectral coverage of the reflectance (250–2500 nm). The proposed name for this result is LESSSR (Lunar Extended Satellite Simulation Solar Reflectance). The E can also refer to EUMETSAT or European [92].

2.9. Overview of Model Performance and Applications

A summary of the performance related to the lunar radiometric model that we have collected through publications or conferences is shown in Table 3, along with a list of some published works on the use of lunar models.

Table 3. Brief summary of the usage range and related studies of the lunar radiometric model.

Model	Publication	Wavelength Coverage (nm)	Phase Angle Coverage (deg)	Uncertainty (Overall Uncertainty)	Related Studies
ROLO (GIRO)	[38]	300–2500	±[2, 92]	5–10% (AP) [2] <1% or 2% (RP) [3]	[22,93–99]
SP	[40,41]	500–1600	±[5, 85]	<1% or 2% (RP)	[22,34,97,99–101]
MT2009	[39]	200–2800 (200–1200) [1]	±[5, 120]	7–17%	[96,102,103]
LIME	[58,104]	340–1640	±[2, 90]	2% (AP) 1% (RP)	[105]
LESSSR	[92]	250–2600	[−80, 20]	~5% (<1.5%, 500–1600 nm)	—
SLIM	[75]	350–2400	±[3, 92]	—	—

[1] Results greater than 1200 nm are based on extrapolation; [2] RP means relative precision; [3] AP means absolute precision.

2.9.1. Model Performance Profile

(1) ROLO: The ROLO program builds on the work on lunar observations carried out by Lane et al. Its direct contribution consists of the formation of an empirical lunar irradiance model using the absolute flux of Vega and the Apollo laboratory reflectance spectra. This allows the prediction of the lunar brightness for different observational configurations using the position of the Sun, Moon, and observer as independent variables [106]. The comprehensive and detailed work to quantify the lunar radiation from ground-based lunar and stellar observations have been widely recognized by the community. Despite the mean absolute fit residuals of approximately 1% for all 32 ROLO bands, the resulting lunar reflectance exhibits some irregular structure, with an estimated model absolute accuracy of only 5–10% [107] and a relative agreement of about 1% [108]. This stems, in part, from the fact that the absolute radiometric response of the ROLO system is anchored in Vega, which has uncertainties of 1.5% and 4% in the VNIR and SWIR regions [52,109]. Furthermore, it has been found to suffer from rapid rotation [110], potentially exacerbating the uncertainty in the Vega reference [111]. Another is inadequate atmospheric characterization, which may lead to an additional uncertainty of ~3% [108], and the ROLO instrument radiometric calibration is influenced by both. In addition, the laboratory reflectance spectra of the Apollo samples are used to characterize the spectral content of the entire lunar disk and as a reference for the adjustment of the ROLO reflectance, which will also introduce some uncertainty [112]. Further, a difference of a few percentage points was also found in extending the spectral smoothing coefficients of a specific viewing geometry to other geometries, and direct fitting of the reflectance to different viewing configurations [58].

Recent lunar observations from Earth-orbiting sensors have revealed residual errors in the ROLO model, mainly manifested as calibration deviations in specific spectral bands during the lunar cycle. Pleiades 1B HR lunar irradiance has found a phase angle dependence approaching 5% in the effective range of the ROLO model [113,114]. Similar features have been observed for the MSG 1/2 SEVIRI, with magnitudes up to 6.1% [115]. The ratio of measurements of Pleiades 1B HR to the simulated irradiance also follows the same trend. On the other hand, Barreto et al. performed nighttime AOD retrievals at the Izaña Observatory using a CE318-T photometer and the lunar Langley method, which relies on ROLO irradiance. This showed a relative difference of >4% [116]. Additional data from geostationary satellites (Himawari-8/9) show that the trend is particularly pronounced at long wavelengths [117]. However, both description and explanation of the deviation pattern are currently inadequate, and new spectrally resolved dense phase angle sampling helps further studies. Several ground-based observations also show differences in the results. The ROLO reflectance is on average about 13% lower than that of observations performed by Velikodsky et al. [118], while the former is in good agreement with the results

of Saiki et al. [119,120]. The most typical application of the model at present remains to detect the response trend over time, although this is somewhat dependent on the observed sequence phase angle. ROLO is reportedly working on reprocessing the data, including using other potential reference stars and improved empirical formulations.

(2) SP: The SP model was developed from the lunar surface mapping of SELENE, incorporating photometric properties to enable its use as a radiance or irradiance model. It also provides comparable lunar images for probes that may view the lunar far side, as expected from a global lunar disk-resolved model. For instrument responses that may contribute to model unreliability, 4 observations at approximately 6-month intervals were used for calibration analysis. They all covered the Apollo 16 reference site with a favorable geological setting (previously used for Clementine data) [121,122]. The results showed that the bias caused by calibration issues is negligible over the SELENE mission [121]. However, in comparison with the ROLO model versus phase angle, they showed different phase angle dependence, such as a good agreement within the phase angle of 30° to 60° at 754.3 nm (<0.5%) and an increase in the small phase angle region ($|\alpha| < 10°$); this pattern also diverges at different wavelengths [41].

In addition, the adopted photometric function omits coherent backscatter opposition effects, coupled with the dramatic reduction in SP observations for large phase angle conditions, restricting the reflectance model to a phase angle range of 5–85°. Furthermore, the SP views the lunar surface under nadir conditions, which prevents the analysis of reflectance properties at larger viewing angles. Consequently, the calibration area for SP simulations is confined to a limited range of lunar surfaces (incident angle < 60° and emission angle < 45°). Therefore, comparisons outside this range may produce higher biases, with image alignment accuracy also contributing. It is worth noting that, to some extent, the current SP model to some extent is traceable to ROLO, which arises from the fact that the spectral slope of SP becomes steeper with increasing wavelength, showing a reddening trend compared to ROLO [123,124]. The SP model cube is available at https://jlpeda.jaxa.jp/product/archive/detail_10/ (accessed on 8 October 2020), but applications to drive the model are not yet publicly available. Additionally, it is reported that Yokota et al. have extended the spectral range of the SP model to NIR2 wavelengths (1007–2600 nm), and validation exercises are ongoing.

(3) MT2009: Another example of developing a lunar irradiance model with multi-source ground-based data is MT2009, a hyperspectral model tailored for VIIRS nighttime multispectral applications, where the standard lookup table version has made operational implementation more accessible. Some nighttime retrievals have also benefited [125,126]. However, the large uncertainty associated with the hyperspectral model is a corollary of the model development philosophy together with objective constraints. First, the data underlying the model were collected from multiple studies and not traceable to identical standards. The lunar phase function was limited to data in 10° increments over a 120° range with a wavelength coverage of 359–1063.5 mm. Next, the non-uniform lunar surface presented the waning side with a larger maria, thus exhibiting an imperfectly symmetrical lunar brightness pattern, and lunar libration results in up to 59% of the visible area [127]. Finally, the model fails to accommodate the opposite effect when the phase is less than 5°, a known issue for models with ground-based data sources.

The overall uncertainty for the irradiance model is in the order of 7–17%, while the irradiance in the phase angle and the wavelength interval that is not accurately modeled is mainly based on extrapolation, and the difference falls at its upper limit. Furthermore, the agreement with the ROLO model is within 5% [39], which meets the application for the low light band at that time; however, it is limited for the sensor calibration.

(4) LIME: The improved LIME is designed to mitigate the uncertainties associated with ROLO traceability to Vega. It builds on the widely used ROLO model and SI-traceable lunar irradiance measurements and puts significant effort into ensuring instrument traceability to SI, from instrument calibration to observation implementation and then to model fitting, with each step including a rigorous uncertainty budget. Model accuracy was estimated

by introducing perturbations caused by instrument and measurement uncertainties and applying Monte Carlo analysis [104]. The uncertainty levels are comparatively consistent across all spectral bands in the CE318-TP9 phase angle range, which they estimate to be less than 2% (k = 2).

Given the Earth-view of lunar observations and the instrumental signal-to-noise ratio, LIME only supports irradiance simulations within a 2–90° phase angle. The model was investigated further with other datasets and models, including Proba-V, Pleiades-1B HR, and Sentinel 3 OLCI, as well as GIRO, and the results suggest that the LIME lunar irradiance is typically around 3–5% higher than the GIRO model for the visible and near-infrared channels. The discrepancy increases with longer wavelengths, along with the possibility that the model may also suffer from phase angle dependence as ROLO does. Moreover, observations from the CE318-TP9 instrument are reported to be ongoing and ideally will be carried out for at least as many periods as the ROLO system, alongside improved reflectance models derived from Pandora spectra and ASD measurements. The LIME model is also receiving continuous validation and refinement, for example, with the results of a space-based observation experiment [128]. The cumulative lunar observations will permit dynamic adjustments to the model.

(5) LESSSR: In addition to the extensive ground-based lunar data, Earth-orbiting lunar observations are also used to investigate lunar reflectance. SCIAMACHY records such data and uses them in a similar form to ROLO for model derivation. Their discrepancies remain consistent over several percentages (typically 5%) and have different phase angle dependencies. Results based on SEVIRI observations show that the former does not exhibit the phase angle pattern at 1640 nm that GIRO has (Figure 24 in [92]). The LESSSR appears to stay reasonably consistent with the GIRO model outside of the effective phase angle of SCIAMACHY, showing only slight phase angle bias. Currently, the model is limited to the effective range of −80° to 20° and is expanding intercomparison activities with models such as GIRO.

(6) SLIM: In contrast to the previous, more isolated data source, SLIM uses observations from multiple instruments. The estimation of the form and the assignment of weights incorporate a large amount of individual judgment, and the final average absolute weighted residual of SLIM is 0.62% [129]. This is approximately half that of the ROLO model. However, the model generated using multi-source observations in turn shows differences when calibrating them, with seven instruments in good agreement with the model at 400–870 nm of approximately 1%. The LIME observed irradiance is 4–7% lower than it, but their absolute uncertainty is 2%. In addition, the ROLO dataset is lower by 5–10%. The Pleiades dense phase angle comparisons and the time series calibration ratios do not exhibit phase angle dependence, but small fluctuations are observed in a single lunation. The calibration results for GEO observations that are not used for model generation are generally more discrete, with some mitigation after attenuation correction. Significant wavelength and phase angle dependence are not observed in the SLIM V1 model apart from the smaller phase angle fluctuations; however, the absolute scale of the model still requires high-precision radiometry.

Several researchers have compared model performance, in addition to the uncertainty budget implemented above. Cao et al. [130] plotted the ratio of MT2009 within the effective phase angle of the GIRO model for the two lunar cycles of November–December 2018 (ratio = MT2009/GIRO). The curve tends to be a logarithmic function with a base greater than 1 at the absolute phase angle, with the ratio increasing monotonically with the phase angle for the waning side and decreasing slightly at ~42° for the waxing side. Agreement is within ±7% for the great majority of the lunar phases, and larger discrepancies outside the range are mainly concentrated in the waning Moon, precisely due to the inability of MT2009 to distinguish the waxing versus waning lunar phases. Moreover, the MT2009 simulations are slightly smaller than GIRO, below 10°. Shao et al. [131] reported the accuracy profile of the MT2009 model predicated on Hyperion lunar observations with typically 5–10% differences in the visible region and a higher variance in irradiance from

the ROLO model for the waning compared with the waxing side. The model-to-model good agreement (5%) lies mainly in visible bands with lunar phases smaller than 30 degrees, and the overall discrepancy pattern depends on the lunar phase and wavelength. Not every model is publicly accessible to date; therefore, further description of the results regarding intercomparison across models has not been covered here.

2.9.2. Application and Refinement Activities

(1) Application: Several published lunar models have been successful in estimating satellite sensor response trends. Of these, the ROLO model received the most widespread adoption, with the classic example being SeaStar SeaWiFS (~7°) [95]. This is followed closely by applications to EO-1 Hyperion (~7°) [132], Aqua/Terra MODIS (~±55.5°) [30], S-NPP VIIRS (~−51°) [29,133], Pleiades HR (~±40°) [134], Proba-V VGT-P (~+7°) [134], Landsat 8 OLI (~+7°) [135], and Terra ASTER (~−27°) [22], which all converge towards the temporal drift monitoring under near-consistent lunar phases. Furthermore, some studies have used the SP model [22,97,99,100], the MT2009 model [96,102], or the recently developed LIME model [105] for parallel validation, either supplemented by other calibration techniques such as SD/SDSM [133,136] or DCC [137,138]. The polar-orbiting and geostationary platform satellite instruments of several agencies accept simulated irradiances from within the uncertainties of the models employed as a relative reference; however, treating the Moon as a cheap but stable object remains the driving force behind the development of its absolute calibration capability.

(2) Refinement activities: The developed lunar models are also being corrected for specific purposes or data sources, and lunar and stellar data acquired by HR attached to the Pleiades constellation are used for phase angle modeling residuals and absolute albedo corrections to the ROLO model [134]. Two that were absolutely traceable to SI exo-atmospheric lunar irradiances were used as potential tie points for the model output, together with SeaWiFS, Pleiades, and VIIRS instrument data to correct the ROLO model [111]. Lunar observations collected by the two MODIS instruments from 2005 to 2012 were also used to improve the ROLO model [139]. Zeng et al. considered libration effects for the MT2009 model with SeaWiFS data [11]. To mitigate possible inaccurate estimates of reflectance caused by changes in gravity and environment where the Apollo return sample exists, the ROLO output results were using the mean equirectangular albedo instead of the reflectance of the mixed sample, following the albedo spectra concluded by [112,118]. Román et al. [140] estimated the Izaña Observatory AOD with lunar photometric measurements under the RIMO (ROLO implementation for Moon's observation) model and, after excluding calibration elements, its apparent discrepancy with the expected value was identified as an inaccuracy of the model value. Therefore, a correction factor was added to the model. Partly Moon-based calibration applications avoid model limitations intentionally. Zhang et al. [141] proposed a cross-calibration with the Moon as an intermediate reference, aiming to mitigate the differences in spectral response. This method fuses the lunar reflectance observed by the reference satellite with the mixed Apollo lunar reflectance to form a hyperspectral reflectance, thus serving as the reference spectrum of the calibrated satellite. Cao et al. [142] developed a lunar band ratio (LBR) method based on two-channel lunar radiation capable of revealing the relative degradation of the instrument without the use of a lunar model. This was implemented upon a reference band with a reliable calibration, usually defined by the ratio of the sum of the offset-removed DNs. It has worked for AVHRR [142], Soumi-NPP VIIRS [143], and MERSI [138], capturing sub-percent inter-band stability and calibrating the band of interest. The LBR between lunar irradiances can also be enforced when lunar models are available.

3. High-Accuracy Lunar Spectral Irradiance Project

Several institutions have progressively developed their lunar models, destined to serve as reliable references within the institution or the calibration community. Within the GSICS framework, models are increasingly being compared against each other to reach

helpful conclusions. Such scenarios entail covering a wide range of viewing geometries and spectral bands. Many sensors have shown excellent on-orbit performance, and several have acted as internal calibration references [144], with observed irradiance being reasonably well consistent with the model. However, such findings are typically carried out in the context of a sparse series of measurements, and they are lacking the spectral regions affected by molecular absorption. In addition, interpretation of the systematic effects concerning the model is inadequate and continues to require an accepted widespread "true" value as an absolute reference. In recent years, lunar measurement campaigns featuring such purposes have been carried out globally (Table 4), dedicated to either temporal or spectral coverage or both, with an order of magnitude improvement in accuracy.

Table 4. The planned and operational typical lunar observation activities.

	Air-LUSI (Air-Based)	MLO-LUSI (Ground-Based)	ARCSTONE (Space-Based)	Lijing (Ground-Based)
Altitude	21.6 km	3397 m	500–600 km	3175 m
Duration	>2 years	>3 years	>3 years	>3 years
Spectral range	350–1100 nm	300–1100 nm	350–2300 nm	400–1000 nm
Spectral resolution	4 nm	3.7 nm	4 nm	2–10 nm
Accuracy goals	<0.5% (k = 1)	<0.5% (k = 1)	<0.5% (k = 1)	<3% (k = 2 early observations)
Funding	NASA/NIST	NIST	NASA	CMA

3.1. Lunar Spectral Irradiance at the Mauna Loa Observatory

NIST has developed a ground-based measurement system for lunar spectral irradiance that works continuously within the visible spectrum. The technique was practiced successfully at the Fred Lawrence Whipple Observatory, demonstrating an uncertainty of better than 1% over 420 to 1000 nm [145]. The Mauna Loa Observatory has been simultaneously proposed as an ideal high-altitude observatory site expected to meet the more stringent uncertainty requirements, which drove the MLO-LUSI (lunar spectral irradiance at Mauna Loa Observatory) and air-LUSI (airborne lunar spectral irradiance) projects described later.

MLO-LUSI is a NIST-sponsored project to establish a lunar observatory at MLO for collecting irradiance at the high-altitude sites, the atmospheric baseline station of NOAA's global monitoring laboratory (GML). The station has continuously monitored and collected data related to atmospheric changes since the 1950s and shares similar observing conditions as the Teide Peak Observatory, with a low and stable AOD suitable for Langley extrapolation.

The MLO-LUSI ground-based radiometric system consists primarily of a telescope coupled with a non-imaging spectrograph, with an integrating sphere with QTH (quartz tungsten halogen) lamps acting as an "artificial moon" allowing continuous calibration and SI traceability to a NIST-calibrated spectrograph. It is expected to carry out 3–5 years of continual observation to obtain dense and accurate irradiance measurements at the proper proportion of the lunar phase and libration cycle, while bridging the gap between the discrete results of the NASA-funded air-LUSI project [146].

MLO has operated two prototype measurement campaigns in 2017 and 2019, with the observatory providing high-quality in situ atmospheric monitoring. It has been reported that the instrument will be fully automated in the near future [147].

3.2. Airborne Lunar Spectral Irradiance

The airborne lunar spectral irradiance (air-LUSI) is a multi-agency collaborative project led by NASA and NIST, dedicated to acquiring spectrally resolved lunar observations at the VNIR region (350–1100 nm) with traceability to SI. This is an active response to the ROLO model lunar phase-related deviations, which will be achieved by low-uncertainty

(~0.5%, k = 1) lunar irradiance observations taken by instruments capable of returning to Earth for calibration.

The air-LUSI mission employs a non-imaging sensor system that has been specifically designed to measure lunar spectral irradiance, sharing an instrument concept with MLO-LUSI and highly complementary to it. It extends the high-altitude site to an aircraft platform above the troposphere, deployed in the wing pod of a NASA ER-2 aircraft, and obtains lunar irradiance measurements of over approximately 95% of the Earth's atmosphere at an operating altitude of about 21.6 km. The integrated autonomous robotic telescope mounted instrument subsystem (ARTEMIS) extracts lunar object information with a tracking camera. It then controls a computer to provide pointing for the telescope [148], locking the Moon at the center of the telescope aperture within a tracking sequence. This is carried out by the two-axis gimbal movement of the well-fixed air-LUSI instrument. ARTEMIS has been proven to have high tracking accuracy and stability (mean RMSE < 0.1°) [149]. NIST-maintained radiometric calibration equipment furnishes metrological standards for the instrument, including lamp-illuminated integrating spheres and transfer standard spectrometers. Routine calibrations are performed pre- and post-flight at the ER-2 hangar for each mission, and an on-board calibration validation source is incorporated into the measurement system; a detailed scheme is available in [150].

Air-LUSI successfully tested the whole observing system during its first engineering flight campaign in 2018. The demonstration flight campaign deployed in 2019 obtained valid data for five nights, with each flight typically consisting of about 45 min of ascent, sustaining nearly 30 min of lunar sampling after turning on the telescope and activating the tracking system. It has a full flight time of about two hours including the descent, covering the 10–60° phase angles of the waning Moon. Except for minor residual atmospheric signature effects, the reflectance converted from air-LUSI irradiance retains the lunar spectral structure, with an uncertainty currently estimated to be better than 1% (450–980 nm) [151]. Lunar disk reflectance shows an agreement of 4–7% in the air-LUSI wavelength range compared to ROLO, and further analysis is still ongoing. A third flight program is expected to capture measurements of the waxing Moon [152].

Air-LUSI alleviates the paradox of rigorous calibrations and atmospheric effects with a return-type platform lunar measurement scheme. The results will serve as a valuable complement of ROLO data or a subset of high-precision measurements to further define lunar calibration models.

3.3. ARCSTONE

ARCSTONE is another NASA-funded demonstration project, also working on using the Moon as a standard reference for Earth-orbiting instruments. This will be accomplished by measuring lunar reflectance in the visible and near-infrared spectral regions at a near-Earth orbit (500–600 km). The ARCSTONE mission is designed to mount a compact spectrometer on the agile 6U CubeSat (a standard small satellite) platform and then sample the Moon with an accuracy of less than 0.5% (k = 1) and at a sufficient density. The instrument measures solar and lunar irradiance with the same imaging scheme and will adopt the temporally close ratio method to minimize potential sensor performance degradation. The difference in magnitude of the target signal is adjusted by high-precision compensation of the integration time and with a pointing accuracy of less than 0.1°. The on-orbit calibration of the ARCSTONE instrument follows the solar cross-calibration technique demonstrated by the prototype instrument of the CLARREO mission, HySICS, to relate SI-traceable solar radiometric scales via measured solar spectral irradiance directly [153].

The ARCSTONE project prototype instrument was designed as a sensor operating in two spectral ranges (UV-VNIR: 348–910 nm; VNIR: 870–2300 nm) [154] and is currently integrated into a single full spectral range instrument to accommodate the compact layout of the CubeSat [155]. The mission intends to allocate at least 3 years of lunar observation duration, with continuous observations of the Moon at a frequency of 12 h when phase angles are below 135° and at positions as far from the equator as possible. Ideally, ARC-

STONE would operate in a strictly polar orbit to approach the limits of lunar latitude libration. The observations of the Sun will be made weekly, at a minimum, and dark-field measurements will be acquired multiple times before and after each lunar and solar measurement sequence. The ARCSTONE mission concept relies on agile maneuvers of the satellite and will yield additional observations outside the phase angle of the ROLO model to support broad phase angle lunar irradiance characterization; the mission is expected to operate in 2024 [156]. Further details on ARCSTONE instrument design, characterization, and mission deployment can be found in [157].

3.4. Lijing Project

The first systematic lunar radiometry in China was organized and led by the National Satellite Meteorological Center of the China Meteorological Administration (CMA/NSMC), jointly with the Changchun Institute of Optics, Fine Mechanics and Physics and the Xi'an Institute of Optics and Precision Mechanics. The primary purpose of the experiment was the inspection and validation of the lunar model while providing the necessary database for model improvement and establishment. The joint experiment has been tested repeatedly at several selected sites in Beijing, Dunhuang, and Lijiang since 2015. Finally, a site near the Lijiang Observatory was chosen, which enjoys both good atmospheric conditions and an annual observable night of about 210 days.

The joint experiment has developed multiple dedicated instruments for lunar spectral irradiance, including both non-imaging and imaging instruments, that are partly still in the process of iterative upgrade. The principal lunar observation instrument is a ground-based lunar imaging spectrometer (GLIS) operating in the 400–1000 nm continuous spectrum (Table 4). The observation system acquires the full disk of radiation using an imaging scheme operating in a passive scanning mode, with Paramount MX+ Equatorial Mounts serving as the instrument's tracking turntable. Each observation night, the instrument is initialized to hold the Moon in the center of FOV by images from an imaging monitor parallel to the GLIS optical axis. The turntable places the instrument on the Moon's track with a 3 min lead time, and the Moon slowly travels through the GLIS slit at roughly 120 to 140 s intervals (limb to limb). The process is performed automatically except for manual intervention during the equatorial instrument flip, and 3 min is the sampling frequency. Details concerning the GLIS design and the operation are found in [158].

The instrument's absolute scale was traceable to the National Institute of Metrology (NIM), China, and was standard through the lamp–plaque system. With the absence of temperature-control devices, the spectrum drift magnitude is estimated from the characteristic spectrum lines under mercury lamp conditions. The lunar spectral irradiance above the atmosphere is based on quasi-synchronous observations of atmospheric properties, including the LIDAR system, the CE318 photometer, and the radiosonde balloon, derived with the aid of the MODTRAN radiative transfer program [159].

The observations from December 2015 to February 2016 experienced complex processing that yielded a lunar spectral irradiance with an uncertainty of sub 3.3%, apart from the atmospheric absorption bands. This was approximately 8.6% higher than the ROLO model. Moreover, the measurements showed a stronger linear relationship between the spectral irradiance ratio and wavelength for the different lunar phases, as did the model, which is related to an effect called phase reddening. The results on phase angle and spectral agreement are available in [160]. The instrument remains operational and accumulated data are being analyzed currently, while its successor is undergoing extensive testing and expects to provide a level of automation well above the GLIS. Additional instruments are less advanced than GLIS due to funding, and other issues and are still in the upgrade and modification phase.

4. SI-Traceable Satellites Lunar Observation Program

Collecting lunar data without atmospheric intrusion on satellite-based platforms remains an ideal approach, which is not technically difficult; however, achieving high quality (low uncertainty) is usually challenging. The proposed climate mission envisages the application of terrestrial metrological reference techniques to space, hence lifting the overall data quality of the EO system. Reliable methods involve putting one or more ultra-high-precision radiometric reference satellites with traceability into suitable orbits, commonly labeled SI-traceable satellites (SITSats) [161], and maintaining highly accurate capabilities over their lifetime. Table 5 summarizes the performance indicators for payloads capable of lunar observation.

Table 5. Key performance parameters for baseline payloads with the capability of lunar measurement (adapted from [162]).

	CLARREO Pathfinder (HySICS)	LIBRA Earth-Moon Imaging Spectrometer (EMIS)	TRUTHS Hyperspectral Imaging Spectrometer (HIS)
Operation	~2023	~2025	~2029
Lifetime	1 year	5–8 years	5–8 years
Platform	International Space Station (ISS)	LIBRA satellite	Small satellite
Orbit	52°	90°	90°
Altitude	400 km	600 km	609 km
Swath width	70 km	50 km	100 km
Spatial resolution	500 m	100 m	50–60 m
Spectral range	350–2300 nm	380–2350 nm	320–2400 nm
Spectral resolution	3 nm	10 nm	4–8 nm
Accuracy goals	0.3% (k = 1)	1% (k = 2)	0.3% (k = 2)

Such satellites offer additional opportunities to approach the actual brightness of the Moon, and indeed lunar viewing will be an essential component of the on-orbit operation for these instruments. Multiple SITSats missions are expected to be highly complementary and promise to provide lunar data with a wide range of viewing geometries. The presence of overlapping samples may also enable intercomparisons across them to fully validate mission SI traceability.

4.1. CLARREO Pathfinder

The Climate Absolute Radiance and Refractivity Observatory (CLARREO) is a demonstration mission developed under the leadership of NASA, consisting of three separate instruments: the infrared (IR) spectrometer, the reflected solar (RS) spectrometer, and the radio occultation (RO) instrument [163,164]. The current primary goal of the mission is to improve the accuracy of on-orbit short-wave and infrared spectroscopy measurements by an order of magnitude and to enable its use as an on-orbit calibration baseline for other Earth-orbiting satellite instruments [165]. It will eventually provide a global initial baseline climate record of at least 5 years [163].

As a precursor demonstration mission, CLARREO Pathfinder (CPF) consists of a high-precision reflected solar spectrometer. It started in 2016 and is scheduled to be officially launched on the ISS in 2023. This represents a crucial step towards a full-scale CLARREO mission to exhibit the critical technologies required for a complete climate observation mission [166].

The CPF RS prototype instrument is the HySICS (Hyperspectral Imager for Climate Science) led by the University of Colorado at Boulder's Laboratory for Atmospheric and Space Physics (LASP). It was designed as a push-broom imaging spectrometer for Earth

that will enable on-orbit SI-traceable observations and deliver radiometric precision below one percent [153]. The CPF payload is planned to be fitted to the ISS Express Logistics Carrier 1 (ELC-1) Site 3 nadir position, enabling 2D pointing capability in the roll and pitch directions, capable of viewing objects such as the Sun, Earth, and Moon by varying the integration time and aperture [167] (Figure 4). The Moon will be imaged in two modes, with the slit perpendicular to the roll or pitch gimbal axis, with the latter achieving cross-slit scanning, which will entail a rotation of the slit projection on the Moon [168]. A typical lunar calibration campaign utilizes the disk-integrated signal from the Moon and therefore requires a solution to the spatial sampling of the rotation.
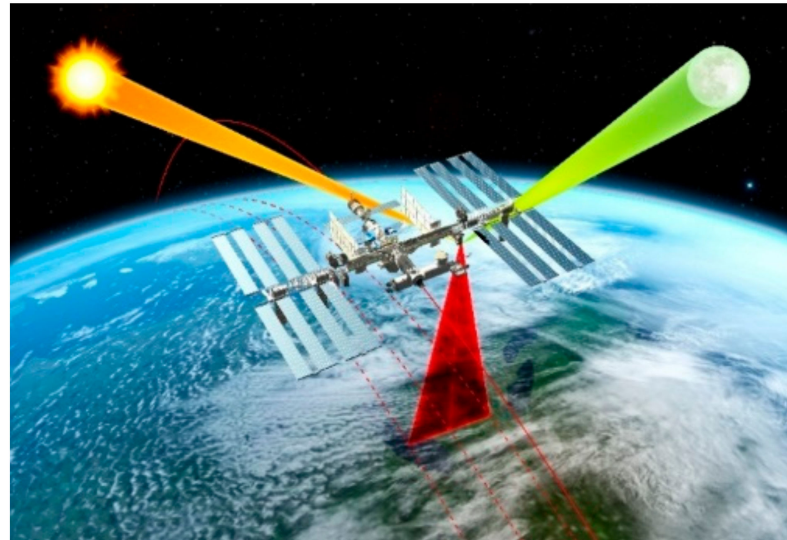
Figure 4. Conceptual view of the CPF HySICS instrument observation aboard the International Space Station [169].

The instrument will start its year-long measurements from the ISS in 2023, with the CPF's FOV limited to the portside of the ISS [108]. It will be constrained by the orbit and attitude adjustment of the station and the movement of components such as solar panels, which may also engage in adaptive attitude maneuvers for the Moon. Stone et al. [168] simulated potential lunar viewing opportunities from the ISS under somewhat ideal contexts, still with a broad time window available to capture a wide range of libration. The hyperspectral lunar record can provide absolute reference for lunar models developed on the basis of ground-based observations, and for such purposes, require the assistance of high-precision data processing techniques. The heart of the mission payload has now been designed and built and is expected to arrive at the ISS on schedule [170].

4.2. TRUTHS

TRUTHS (Traceable Radiometry Underpinning Terrestrial- and Helio-Studies) is a UK-proposed climate-focused mission that has been integrated into the ESA Earth observation program towards a space-based climate and calibration system traceable to SI. This aims to achieve two main objectives: (1) the direct collection of sufficiently accurate reference datasets, and (2) the transfer of space reference standards to other on-orbit sensors [165,171,172].

The main imaging instrument of TRUTHS is the hyperspectral imaging spectrometer (HIS), which extends the continuous spectrum to the UVA. The mission considers a small agile satellite of approximately 1 m^3 as a carrier [173], which will directly view the Earth, Sun, and Moon via the HIS sensor (Figure 5).

Figure 5. TRUTHS HIS instrument on-orbit observation concept diagram [174].

The SI traceability chain of the TRUTHS radiometric calibration system replicates the typical strategy of the terrestrial metrology technology, with the cryogenic solar absolute radiometer (CSAR) at its core, which is an electrically substituted radiometer for operation in the vacuum of space. The prototype was launched in 2010 and, following improvements and a simplified design, a second version with a lower mass was completed in 2016, which can be easily adapted for a flexible platform. The CSAR is expected to operate at temperatures below 60 K due to the limitations of the on-orbit space cooler, and a detailed description of the calibration sequence can be found in [171].

4.3. LIBRA

The Chinese Space-based Radiometric Benchmark (CSRB) project aims to launch a reference-type satellite named LIBRA, which will be realized by four basic payloads, namely an infrared spectrometer (IRS) with high spectral resolution, an Earth–Moon imaging spectrometer (EMIS) to measure reflected solar radiation, a total solar irradiance (TSI) instrument, and a solar spectral irradiance monitoring instrument traceable to quantum benchmark (SITQ). The space-based micro-scale standards laboratory is also highly integrated, allowing direct on-orbit traceability of satellite radiometric observations to the SI [162,175].

The EMIS is mounted on a two-axis gimbal and features an optical design consisting of a telescope and a hyperspectral imaging spectrometer. This allows for multiple scenarios of observations in different modes, with the Moon designed as the routine object of observation. On-orbit traceability of EMIS is achieved through the space cryogenic absolute radiometer (SCAR) (refer to Figure 3 in [162] for a schematic of the SI traceability chain), which works as an electrically substituted radiometer at a 20 K operating temperature. The prototype started in 2015, and uncertainty analysis showed that the SCAR of the first version was much better than 1% [175,176].

With its optimized trajectory design and agile observation capabilities, LIBRA will enable quasi-synchronous observation with other operational sensors, besides the collection of regular observations. SI-traceable sampling of the lunar radiation will be made at high spectral resolution from vantage points in the visible region of the Moon, enabling intercalibration independent of the standard lunar model with the aid of a reference satellite (Figure 6). The reliable lunar calibration reference, once available, will provide a third-party reference. The LIBRA mission is not exclusively limited to dedicated satellites; a scaled-down version of LIBRA with simplified mission elements also takes the China Space Station (CSS) and the agile satellites as potential platforms to work on sub-missions.
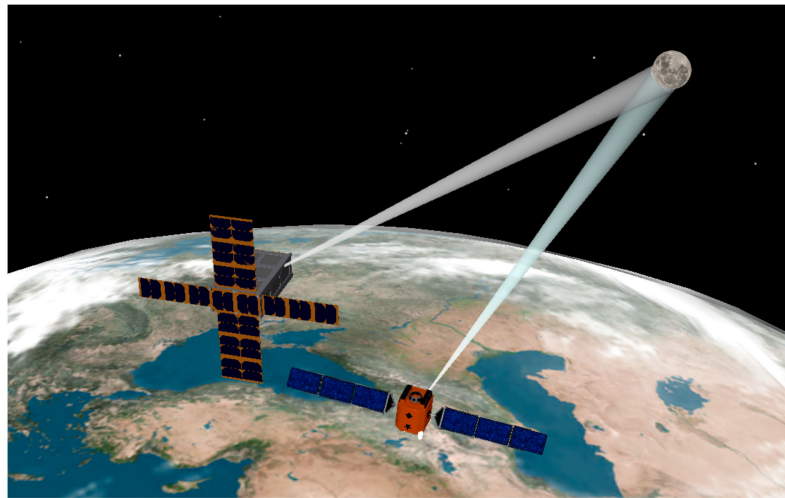
Figure 6. LIBRA EMIS lunar observation and transfer calibration schematic.

5. Discussion

The original calibration reference model has been operational for 18 years to date and has contributed significantly to the calibration community, representing the most accurate knowledge of lunar disk photometry available. However, the natural limitations of the ROLO system have rendered the most commonly used lunar model unable to provide absolute response estimates with less than a 5% uncertainty. Models developed subsequently have partially addressed some of the consensus issues, mostly as local solutions specific to particular objectives. A range of embodied activities and mission concepts dedicated to improving at least a certain aspect is in progress in anticipation of recording a sufficient volume of high-confidence observations for absolute lunar reference. We have presented a summary of some fundamental issues from both the data and model layers.

5.1. Data Fusion

The acquisition of low-uncertainty lunar data and the large number of observations accumulated will serve the common goal. The dataset should be complementary (containing various sampling mechanisms, spatial and spectral resolutions, observational geometries from different sensors, and also non-imaging types). However, these sensors are usually not synchronous, and mutual comparison and standard transfer of synchronous observations would be highly beneficial. On the other hand, image processing techniques may need to be revisited, and differences between lunar reference and other calibration results understood to render the results truly usable. This typically involves spatial integration of Moon radiance images across the entire lunar disk and assessment of instrument effects (e.g., oversampling and background subtraction, which can be affected by lunar phases). Finding a general procedure that applies to all instrument characteristics takes a lot of work; however, guidelines or specifications for normalizing particular critical techniques are feasible since even different instruments face general problems. Therefore, in-depth data analysis should follow certain guidelines so that the results reflect the response to the lunar source fully. In addition, these guidelines need to cover aspects other than technology; it has been found that errors or inconsistencies among multiple agencies often accompany specific calculations, and unification should be developed within the community on basic parameters, such as the ephemeris files used and methods or tools for calculating photometric angles. Incremental improvements in methods and results have contributed to a clearer understanding of lunar radiative variability.

5.2. Model Formulation

Inadequate analytical forms or imperfect parameter solutions will ultimately degrade model performance, and to date, many Earth-perspective lunar observations have been accumulated. Furthermore, the data collected are still limited for lunar orbiter missions, but many empirical or semi-empirical and physical photometric models have been proposed [120]. Meanwhile, the data handling capabilities of the computational system have been greatly enhanced. The assembled observations have provided the possibility to simulate the lunar reflectance using deep learning methods, especially for disk-equivalent albedo. Previous physics- or empirical-based models can be combined with recently developed deep learning methods to aid in finding optimal solutions from a substantial sample of lunar observations. SLIM assimilates multi-source data to iterate the model in a very close to learning-based approach and adopts a feature-scaling-like scheme for improving the numerical stability of the fit. Several current neural network algorithms have explicit feature cross capabilities, which help to improve nonlinear mapping capabilities and are potentially superior to traditional methods. Furthermore, model-based datasets are available to some extent as supplementary data, which are validated for their uncertainty. The introduction of such state-of-the-art methods should include extensive accuracy assessment and rich archived data to enable full validation of model generalization capabilities. Further, the ability to run the model independently facilitates the implementation of broad comparison. Consensus models will inevitably be built on extensive validation, and a parallel simplified model may be required to meet specific applications. On the other hand, efforts to improve the accuracy of lunar models at this stage are compensated by collecting data with low uncertainties, including observations from multiple platforms in terrestrial space. Several spacecraft-based optical studies methods, such as the phase ratio and color ratio, can be naturally introduced into such observations [120]. Earth-based and spacecraft observations have yielded several beneficial results in global and regional measurements [118,123,177,178]; for example, Berezhnoi et al. [179] calculated the small lunar area reflectance based on the empirical phase dependence of the lunar spectral slope in the visible near-infrared region obtained by Korokhin et al. [177].

5.3. Radiance of Specific Parts

The disk-integrated model simplifies the lunar reference, which involves irradiance extraction techniques. When using the Moon as an optical standard for Earth-orbiting satellites, a comprehensive observation of the Moon is required to use these models. Several current models provide a summation of the radiance on the Moon's nearside. It is impractical to use them for calibration based on small FOV instruments or for local observations and for vestigial observations of instruments that can accommodate the Moon. When turning to optical studies of the Moon, lunar phase photometry based on spacecraft measurements has a long history [120,180]. However, observations from terrestrial space are not profoundly linked to those from lunar orbiters at the calibration level, with one focusing on the lunar surface's detailed physical and chemical properties and the other's focusing on evaluating the instrument's performance. Nevertheless, a typical process for them is to address absolute reflectance. Several instruments can obtain spatially resolved Moon views, and identifying the specific homogeneous regions is possible to facilitate the study of local photometric properties of the lunar surface, thus allowing the development of radiometric calibration schemes for such instruments. However, no calibration references are available for small lunar regions [179], especially for Earth-orbiting satellites.

The lunar brightness is highly dependent on the photometric angle, as are the local regions, so similar difficulties are present for the calibration using small regions. When data collected by different instruments have similar geometry in specified areas, the observations can be directly comparable based on positions accurately referencing the lunar coordinate system (selenographic coordinate). However, the estimated geometrical differences between terrestrial space and spacecraft missions are large, and their respective measurements are expected to generate larger comparable areas. On the other hand, lunar

orbiter measurements can be used as a reference and are not restricted to the limited or even zero-matching region described above. Again, this requires consistent geometries, and their agreement is not native and is usually obtained by photometric model simulations derived from lunar orbital data. Such a process adjusts the standard geometry to the measurement geometry. The latter relies heavily on the approximate expression of lunar directional reflectance and also needs to consider the resolution matching problem. A significant advantage of this is finding multiple sets of suitable regions with different brightness levels on the lunar surface, with the prerequisite that the observed images be mapped to the lunar coordinate system. The image point, object point, and projection center in one central projection are co-linear and strictly follow the geometric sensor model. Therefore, completing the projection following the imaging geometry with the imaging system knowledge and the simultaneous recording state as the interior and exterior orientation elements is suitable for lunar observations. The second one is a lightweight method for solving the lunar surface position. When the satellite is imaged in the mean Earth direction of the Moon, the imaging plane is precisely perpendicular to the lunar equatorial plane. Thus, the nominal lunar surface coordinates (longitude and latitude range between -90 degrees and $+90$ degrees) constructed for the actual image can be used as the starting point. The mapping from the nominal image to the observed image can be completed by solving the problem of the libration and the diversity of the Moon into the instrument's FOV during the satellite observation. The calibrated target reflectance can be used as a radiometric baseline for the instrument's performance.

5.4. Usage Policy

Reaching a consensus model may take time, but there is still an ongoing effort to follow up on this, which entails a concerted effort by the calibration community; GSICS will continue to play an important role. The outcome should be made public and shared within a policy framework while considering the portability of future lunar models as well as the ease of use, thus expanding the impact of lunar calibration. A clear vision is to enhance the interoperability of sensor-derived products, and robust models will ensure that the various types of data acquired from the sensors are linked to a common reference. As several issues are progressively resolved, the instruments that benefit from it will provide more consistent science-grade data to enable a clear portrayal of the rate and magnitude of the global target change, allowing users to focus more on algorithms for more advanced data products.

6. Conclusions

Lunar viewing has become almost the standard configuration for EO satellites to be launched, and lunar calibration will undoubtedly be an essential component of the vicarious calibration strategy for them. In this paper, we have attempted to summarize the lunar disk reflectance characterization algorithms since 2000, each with its own set of procedures and using the collected set of data. In addition, high-precision lunar observation campaigns have been increasing in the last decade. Briefly, we reviewed and summarized systematically the radiometric model of the Moon as an absolute calibration source and the accompanying and derived observational activities. We have classified these into three phases based on the development of the lunar radiometric model, reflecting the efforts made by past, current, and future missions. The timeline of development shown in this paper has allowed us to gain insight into the current status and to recognize and revisit present-day work.

While much work has been undertaken on describing the absolute lunar reflectance using different data platforms, the data from the Earth perspective have yet to be combined much with the extensive information obtained by many lunar missions. Their observations have strengths and limitations, for example, the Earth-based observations cannot obtain valid information on the absorption band and the phase interval of the opposition effects. Several methods or results from studying the lunar surface using spacecraft can be extended to observing the lunar nearside. In addition, the lunar data collected in terrestrial space

at this stage far exceed those gathered by spacecraft missions; they are also gradually approaching the true lunar brightness, and biases in some data or models are known. When these datasets are combined with neural-network-based methods, they can be compared as complementary or independent approaches.

The use of lunar calibration for most instruments at this stage may be due to economic and practical reasons. If the resulting lunar calibration model is not conducive to propagation or is not referenced to the same standard, it means that interoperability between data remains limited. Therefore, there is a need for a generic and easy-to-operate model that is used on a broader scale. As an opposite process, one should simultaneously focus on the uncertainty of the acquired measurements. It is highly recommended to regulate the analysis techniques in lunar irradiance. The specification needs to impose restrictions on specific generic procedures and underlying data to eliminate inconsistencies between the results caused by them.

Although the Moon as a calibration source promises to provide an absolute reference, the lunar signal is typically at the low side of the instrument's radiometric response. It is suitable for characterizing the instrument's performance in the low dynamic range. Moreover, lunar data acquisition typically occurs from the first quarter to the third quarter of the lunar phase, thus lacking data for half of the lunar cycle. Overall, relying only on lunar targets to complete instrument calibration for full or wide dynamic ranges is impractical, while some instruments have a strong nonlinear response. There are also no well-behaved regional calibration models when considering photometric knowledge of small lunar regions with different brightness levels. Therefore, combining existing and parallel developed calibration methods will provide better results than individual targets.

Satellite observations are an excellent way to perceive climate variables, and the climate is a typically complex system. In the same way, understanding the lunar brightness behavior would be better supported by accurate and consistent datasets, which requires a combination of time series results from different instruments. The Moon provides an ideal reference for this and is several orders of magnitude greater than any EO satellite stability scale. The calibration community has developed several useful lunar models, and a couple of high-precision observation projects are running smoothly, exploiting the full potential of the Moon as a spatial reference. From the successful practice of existing lunar models, the expected outcome would be a generally accepted consensus model bound to lunar irradiance and built on extensive validation by various instruments. At the same time, expanding constellations of small satellites are driving changes in Earth observation, and in the near future, lunar calibration methods will be used entirely as commercial constellations for full-life operational monitoring.

References

1. Tatem, A.J.; Goetz, S.J.; Hay, S.I. Fifty years of Earth-observation satellites—Views from space have led to countless advances on the ground in both scientific knowledge and daily life. *Am. Sci.* **2008**, *96*, 390–398. [CrossRef] [PubMed]
2. GCOS. The Global Observing System for Climate: Implementation Needs. Available online: https://library.wmo.int/doc_num.php?explnum_id=3417 (accessed on 12 November 2021).
3. Meygret, A.; Blanchet, G.; Latry, C.; Kelbert, A.; Gross-Colzy, L. On-orbit star-based calibration and modulation transfer function measurements for PLEIADES high-resolution optical sensors. *IEEE Trans. Geosci. Remote Sens.* **2019**, *57*, 5525–5534. [CrossRef]
4. Xiong, X.; Aldoretta, E.; Angal, A.; Chang, T.; Geng, X.; Link, D.; Salomonson, V.; Twedt, K.; Wu, A. Terra MODIS: 20 years of on-orbit calibration and performance. *J. Appl. Remote Sens.* **2020**, *14*, 037501. [CrossRef]
5. Sterckx, S.; Brown, I.; Kääb, A.; Krol, M.; Morrow, R.; Veefkind, P.; Boersma, K.F.; De Mazière, M.; Fox, N.; Thorne, P. Towards a European Cal/Val service for Earth observation. *Int. J. Remote Sens.* **2020**, *41*, 4496–4511. [CrossRef]
6. Goldberg, M.; Ohring, G.; Butler, J.; Cao, C.; Datla, R.; Doelling, D.; Gaertner, V.; Hewison, T.; Iacovazzi, B.; Kim, D.; et al. The global space-based inter-calibration system. *Bull. Am. Meteorol. Soc.* **2011**, *92*, 467–475. [CrossRef]
7. Belward, A. International co-operation in satellite sensor calibration: The role of the CEOS working group on calibration and validation. *Adv. Space Res.* **1999**, *23*, 1443–1448. [CrossRef]
8. Sun, L.; Hu, X.; Guo, M.; Xu, N. Multisite calibration tracking for FY-3A MERSI solar bands. *IEEE Trans. Geosci. Remote Sens.* **2012**, *50*, 4929–4942. [CrossRef]
9. Helder, D.; Thome, K.J.; Mishra, N.; Chander, G.; Xiong, X.; Angal, A.; Choi, T. Absolute radiometric calibration of Landsat using a pseudo invariant calibration site. *IEEE Trans. Geosci. Remote Sens.* **2013**, *51*, 1360–1369. [CrossRef]
10. Chander, G.; Xiong, X.; Choi, T.; Angal, A. Monitoring on-orbit calibration stability of the Terra MODIS and Landsat 7 ETM+ sensors using pseudo-invariant test sites. *Remote Sens. Environ.* **2010**, *114*, 925–939. [CrossRef]
11. Zeng, X.; Shao, X.; Qiu, S.; Ma, L.; Gao, C.; Li, C. Stability monitoring of the VIIRS Day/Night Band over Dome C with a lunar irradiance model and BRDF correction. *Remote Sens.* **2018**, *10*, 189. [CrossRef]
12. Xiong, X.; Wu, A.; Wenny, B.N. Using Dome C for moderate resolution imaging spectroradiometer calibration stability and consistency. *J. Appl. Remote Sens.* **2009**, *3*, 033520.
13. Wang, L.; Hu, X.; Zheng, Z.; Chen, L. Radiometric calibration tracking detection for FY-3A/MERSI by joint use of snow targets in south and north poles. *Acta Opt. Sin.* **2018**, *38*, 0212003. (In Chinese) [CrossRef]
14. Heidinger, A.K.; Cao, C.Y.; Sullivan, J.T. Using Moderate Resolution Imaging Spectrometer (MODIS) to calibrate Advanced Very High Resolution Radiometer reflectance channels. *J. Geophys. Res. Atmos.* **2002**, *107*, AAC-11-1–AAC-11-10. [CrossRef]
15. Hewison, T.J.; Wu, X.; Yu, F.; Tahara, Y.; Hu, X.; Kim, D.; Koenig, M. GSICS inter-calibration of infrared channels of geostationary imagers using Metop/IASI. *IEEE Trans. Geosci. Remote Sens.* **2013**, *51*, 1160–1170. [CrossRef]
16. Sun, J.; Chu, M.; Wang, M. Degradation nonuniformity in the solar diffuser bidirectional reflectance distribution function. *Appl. Opt.* **2016**, *55*, 6001–6016. [CrossRef] [PubMed]
17. Farhad, M.M.; Kaewmanee, M.; Leigh, L.; Helder, D. Radiometric cross calibration and validation using 4 angle BRDF model between Landsat 8 and Sentinel 2A. *Remote Sens.* **2020**, *12*, 806. [CrossRef]
18. Wu, A.; Geng, X.; Wald, A.; Angal, A.; Xiong, X. Assessment of Terra MODIS on-orbit polarization sensitivity using pseudoinvariant desert sites. *IEEE Trans. Geosci. Remote Sens.* **2017**, *55*, 4168–4176. [CrossRef]
19. Chander, G.; Helder, D.L.; Aaron, D.; Mishra, N.; Shrestha, A.K. Assessment of spectral, misregistration, and spatial uncertainties inherent in the cross-calibration study. *IEEE Trans. Geosci. Remote Sens.* **2013**, *51*, 1282–1296. [CrossRef]
20. Wu, C.; Qi, C.; Hu, X.; Gu, M.; Yang, T.; Xu, H.; Lee, L.; Yang, Z.; Zhang, P. FY-3D HIRAS radiometric calibration and accuracy assessment. *IEEE Trans. Geosci. Remote Sens.* **2020**, *58*, 3965–3976. [CrossRef]
21. Bhatt, R.; Doelling, D.R.; Wu, A.; Xiong, X.; Scarino, B.R.; Haney, C.O.; Gopalan, A. Initial stability assessment of S-NPP VIIRS reflective solar band calibration using invariant desert and deep convective cloud targets. *Remote Sens.* **2014**, *6*, 2809–2826. [CrossRef]
22. Kouyama, T.; Kato, S.; Kikuchi, M.; Sakuma, F.; Miura, A.; Tachikawa, T.; Tsuchida, S.; Obata, K.; Nakamura, R. Lunar calibration for ASTER VNIR and TIR with observations of the Moon in 2003 and 2017. *Remote Sens.* **2019**, *11*, 2712. [CrossRef]
23. Santer, R.; Martiny, N.; Cabot, F. Two different approaches to achieve vicarious calibration without a priori on the aerosol model: Application to SPOT5 over the test site of La Crau, France. In Proceedings of the Sensors, Systems, & Next-Generation Satellites VII, Barcelona, Spain, 8–12 September 2003; pp. 456–467.
24. Obata, K.; Tsuchida, S.; Iwao, K. Inter-band radiometric comparison and calibration of ASTER visible and near-infrared bands. *Remote Sens.* **2015**, *7*, 15140–15160. [CrossRef]
25. Kieffer, H.H. Photometric stability of the lunar surface. *Icarus* **1997**, *130*, 323–327. [CrossRef]
26. Kieffer, H.; Wildey, R. Absolute calibration of Landsat instruments using the Moon. *Photogramm. Eng. Remote Sens.* **1985**, *51*, 1391–1393.
27. Wilson, T.; Angal, A.; Xiong, X. Orbital path and spacecraft attitude correction for the MODIS lunar spatial characterization. *IEEE Trans. Geosci. Remote Sens.* **2020**, *58*, 1063–1073. [CrossRef]
28. Wilson, T.; Xiong, X. Planning lunar observations for satellite missions in low-Earth orbit. *J. Appl. Remote Sens.* **2019**, *13*, 024513. [CrossRef]
29. Wang, Z.; Xiong, X.; Fulbright, J.; Lei, N. VIIRS Day/Night Band radiometric calibration stability monitoring using the Moon. *J. Geophys. Res. Atmos.* **2017**, *122*, 5616–5624. [CrossRef]

30. Sun, J.Q.; Xiong, X.; Barnes, W.L.; Guenther, B. MODIS reflective solar bands on-orbit lunar calibration. *IEEE Trans. Geosci. Remote Sens.* **2007**, *45*, 2383–2393. [CrossRef]

31. Wu, R.; Zhang, P.; Xu, N.; Hu, X.; Chen, L.; Zhang, L.; Yang, Z. FY-3D MERSI on-orbit radiometric calibration from the lunar view. *Sensors* **2020**, *20*, 4690. [CrossRef]

32. Wu, R.; Zhang, P.; Zheng, X.; Hu, X.; Xu, N.; Zhang, L.; Qiao, Y. Data collection and irradiance conversion of lunar observation for MERSI. *Opt. Precis. Eng.* **2019**, *27*, 1819–1827. (In Chinese)

33. Change, C. Achieving Satellite Instrument Calibration for Climate Change (ASIC3). Available online: http://wcrp.ipsl.jussieu.fr/Documents/ACC/WOAP/WOAP_SatelliteObs4CC2007.pdf (accessed on 3 October 2021).

34. Kouyama, T.; Nakamura, R.; Kato, S.; Miyashita, N. One-year lunar calibration result of Hodoyoshi-1, Moon as an ideal target for small satellite radiometric calibration. In Proceedings of the Small Satellite Conference, Logan, UT, USA, 4–9 August 2018.

35. Roux, J.; Christopher, S.; Maskey, M. Exploring the use of PlanetScope data for particulate matter air quality research. *Remote Sens.* **2021**, *13*, 2981. [CrossRef]

36. Young, C.L.; Lukashin, C.; Taylor, P.C.; Swanson, R.; Kirk, W.S.; Cooney, M.; Swartz, W.H.; Goldberg, A.; Stone, T.; Jackson, T.; et al. Trutinor: A conceptual study for a next-generation Earth radiant energy instrument. *Remote Sens.* **2020**, *12*, 3281. [CrossRef]

37. Wagner, S.C.; Hewison, T.; Stone, T.; Lachérade, S.; Fougnie, B.; Xiong, X. A summary of the joint GSICS—CEOS/IVOS lunar calibration workshop: Moving towards intercalibration using the Moon as a transfer target. In Proceedings of the Sensors Systems, & Next-Generation Satellites XIX, Toulouse, France, 21–24 September 2015; p. 96390Z.

38. Kieffer, H.H.; Stone, T.C. The spectral irradiance of the Moon. *Astron. J.* **2005**, *129*, 2887–2901. [CrossRef]

39. Miller, S.D.; Turner, R.E. A dynamic lunar spectral irradiance data set for NPOESS/VIIRS Day/Night Band nighttime environmental applications. *IEEE Trans. Geosci. Remote Sens.* **2009**, *47*, 2316–2329. [CrossRef]

40. Yokota, Y.; Matsunaga, T.; Ohtake, M.; Haruyama, J.; Nakamura, R.; Yamamoto, S.; Ogawa, Y.; Morota, T.; Honda, C.; Saiki, K.; et al. Lunar photometric properties at wavelengths 0.5–1.6 μm acquired by SELENE Spectral Profiler and their dependency on local albedo and latitudinal zones. *Icarus* **2011**, *215*, 639–660. [CrossRef]

41. Kouyama, T.; Yokota, Y.; Ishihara, Y.; Nakamura, R.; Yamamoto, S.; Matsunaga, T. Development of an application scheme for the SELENE/SP lunar reflectance model for radiometric calibration of hyperspectral and multispectral sensors. *Planet. Space Sci.* **2016**, *124*, 76–83. [CrossRef]

42. Lane, A.P.; Irvine, W.M. Monochromatic phase curves and albedos for the lunar disk. *Astron. J.* **1973**, *78*, 267–277. [CrossRef]

43. Young, A.T.; Irvine, W.M. Multicolor photoelectric photometry of the brighter planets. I. Program and Procedure. *Astron. J.* **1967**, *72*, 945–950. [CrossRef]

44. King, I. Effective extinction values in wide-band photometry. *Astron. J.* **1952**, *57*, 253. [CrossRef]

45. Buratti, B.J.; Hiller, J.K.; Wang, M. The lunar opposition surge: Observations by Clementine. *Icarus* **1996**, *124*, 490–499. [CrossRef]

46. Hapke, B.W.; Nelson, R.M.; Smythe, W.D. The opposition effect of the Moon—The contribution of coherent backscatter. *Science* **1993**, *260*, 509–511. [CrossRef] [PubMed]

47. Peacock, K. Multicolor photoelectric photometry of the Lunar surface. *Icarus* **1968**, *9*, 16–66. [CrossRef]

48. Wildey, R.L.; Pohn, H.A. Detailed photoelectric photometry of the Moon. *Astron. J.* **1964**, *69*, 619. [CrossRef]

49. Roberts, G.L. Three-color photoelectric photometry of the Moon. *Icarus* **1966**, *5*, 555–564. [CrossRef]

50. Anderson, J.M.; Becker, K.J.; Kieffer, H.H.; Dodd, D.N. Real-time control of the robotic lunar observatory telescope. *Publ. Astron. Soc. Pac.* **1999**, *111*, 737. [CrossRef]

51. Stone, T.C.; Kieffer, H.H. Absolute irradiance of the Moon for on-orbit calibration. In Proceedings of the Conference on Earth Observing Systems VII, Seattle, WA, USA, 7–11 July 2002; pp. 211–221.

52. Strecker, D.W.; Erickson, E.F.; Witteborn, F.C. Airborne stellar spectrophotometry from 1.2 to 5.5 microns: Absolute calibration and spectra of stars earlier than M3. *Astrophys. J. Suppl. Ser.* **1979**, *41*, 501–512. [CrossRef]

53. Hayes, D.S.; Pasinetti, L.E.; Philip, A.D. *Calibration of Fundamental Stellar Quantities: Proceedings of the 111th Symposium of the International Astronomical Union, Como, Italy, 24–29 May 1984*; Springer Science & Business Media: Berlin/Heidelberg, Germany, 2012.

54. Castelli, F.; Kurucz, R.L. Model atmospheres for Vega. *Astron. Astrophys.* **1994**, *281*, 817–832.

55. Stone, T.C.; Kieffer, H.H.; Anderson, J.M. Status of use of lunar irradiance for on-orbit calibration. In Proceedings of the Conference on Earth Observing Systems VI, San Diego, CA, USA, 29 July–3 August 2001; pp. 165–175.

56. Lucey, P.G.; Hawke, B.R.; Pieters, C.M.; Head, J.W.; McCord, T.B. A compositional study of the Aristarchus region of the Moon using near-infrared reflectance spectroscopy. *J. Geophys. Res. Solid Earth* **1986**, *91*, 344–354. [CrossRef]

57. Pieters, C.M.; Mustard, J.F. Exploration of crustal/mantle material for the Earth and Moon using reflectance spectroscopy. *Remote Sens. Environ.* **1988**, *24*, 151–178. [CrossRef]

58. Sarah, T.; Emma, W.; Andrew, B.; Stefan, A.; Carlos, T.; Africa, B.; Alberto, B. D1: Strategy for the Derivation of an Improved Lunar Spectral Irradiance Model Based on Lunar Photometer Measurements. Available online: https://calvalportal.ceos.org/lime (accessed on 12 September 2021).

59. Pieters, C.M. The Moon as a spectral calibration standard enabled by lunar samples: The Clementine example. In Proceedings of the Workshop on New Views of the Moon II: Understanding the Moon through the Integration of Diverse Datasets, Flagstaff, AZ, USA, 22–24 September 1999; pp. 47–48.

60. Viticchie, B.; Stone, T.; Wagner, S.; Takahashi, M.; Hewison, T. Preparation of the GIRO Executable. Available online: http://gsics.atmos.umd.edu/pub/Development/20140916/2_GIRO_preparation_second_webmeeting.pptx (accessed on 10 September 2021).

61. Wagner, S.; Hewison, T.; Stone, T.; Lachérade, S.; Fougnie, B.; Xiong, J. Outcome of the GSICS/CEOS-IVOS Lunar Calibration Workshop. Available online: https://digitalcommons.usu.edu/calcon/CALCON2015/All2015Content/47/ (accessed on 16 May 2021).

62. EUMETSAT. High Level Description of the GIRO Application and Definition of the Input/Output Formats. Available online: http://gsics.atmos.umd.edu/pub/Development/LunarWorkArea/GSICS_ROLO_HighLevDescript_IODefinition.pdf (accessed on 1 March 2020).

63. Shaw, J.A. Modeling infrared lunar radiance. *Opt. Eng.* **1999**, *38*, 1763–1764. [CrossRef]

64. Younkin, R.L. Optical reflectance of local areas of the Moon. *Astron. J.* **1970**, *75*, 831–840. [CrossRef]

65. Lawrence, S.J.; Lau, E.; Steutel, D.; Stopar, J.D.; Wilcox, B.B.; Lucey, P.G. A new measurement of the absolute spectral reflectance of the Moon. In Proceedings of the 34th Lunar and Planetary Science Conference, League City, TX, USA, 17–21 March 2003; p. 1269.

66. Nozette, S.; Rustan, P.; Pleasance, L.P.; Horan, D.M.; Regeon, P.; Shoemaker, E.M.; Spudis, P.D.; Acton, C.H.; Baker, D.N.; Blamont, J.E.; et al. The Clementine mission to the Moon: Scientific overview. *Science* **1994**, *266*, 1835–1839. [CrossRef] [PubMed]

67. Kato, M.; Takizawa, Y.; Sasaki, S. The SELENE (Kaguya) mission: Present status and preliminary science. In Proceedings of the 37th COSPAR Scientific Assembly, Montréal, QC, Canada, 13–20 July 2008; p. 1463.

68. Sun, H.; Wu, J.; Dai, S.; Zhao, B.; Shu, R.; Chang, J.; Wang, H.; Zhang, X.; Ren, Q.; Chen, X.; et al. Introduction to the payloads and the initial observation results of Chang'E-1. *Chin. J. Space Sci.* **2008**, *28*, 374–384.

69. Goswami, J.N. An overview of the Chandrayaan-1 mission. In Proceedings of the 41st Annual Lunar and Planetary Science Conference, Houston, TX, USA, 1–5 March 2010.

70. Sobue, S.-I.; Sasaki, S.; Kato, M.; Maejima, H.; Minamino, H.; Konishi, H.; Otake, H.; Nakazawa, S.; Tateno, N.; Hoshino, H. The result of SELENE(KAGUYA) development and operation. *Recent Patents Space Technol.* **2009**, *1*, 12–22. [CrossRef]

71. Ohtake, M.; Haruyama, J.; Matsunaga, T.; Yokota, Y.; Morota, T.; Honda, C.; Team, L. Performance and scientific objectives of the SELENE (KAGUYA) Multiband Imager. *Earth Planet. Space* **2008**, *60*, 257–264. [CrossRef]

72. Mcewen, A.S. A precise lunar photometric function. In Proceedings of the Lunar and Planetary Science Conference, Houston, TX, USA, 18–22 March 1996; pp. 841–842.

73. Mcewen, A.; Eliason, E.; Lucey, P.; Malaret, E.; Sucharski, T. Summary of radiometric calibration and photometric normalization steps for the clementine UVVIS images. In Proceedings of the 29th Annual Lunar and Planetary Science Conference, Houston, TX, USA, 16–20 March 1998.

74. Yokota, Y.; Honda, R.; Iijima, Y.; Mizutani, H. New method of photometric correction for lunar UVVIS images. In Proceedings of the 34th Annual Lunar and Planetary Science Conference, League City, TX, USA, 17–21 March 2003.

75. Kieffer, H.H. Multiple-instrument-based spectral irradiance of the Moon. *J. Appl. Remote Sens.* **2022**, *16*, 038502. [CrossRef]

76. Kieffer, H.; Stone, T. A Model of the Spectral Irradiance of the Moon for Calibration of Earth-Orbiting Spacecraft Instruments. Available online: https://citeseerx.ist.psu.edu/document?repid=rep1&type=pdf&doi=7299ea94db402100489bc6b4dfbea63b31866b15 (accessed on 10 March 2020).

77. Kieffer, H. Seeking a Consensus Evolutionary Lunar Calibration Model, Many Observations, One Moon. Available online: https://digitalcommons.usu.edu/calcon/CALCON2019/invitedspeaker/1/ (accessed on 6 April 2020).

78. Kieffer, H. A Lunar Calibration Model Based on Many Instruments and One Moon. Available online: https://digitalcommons.usu.edu/calcon/CALCON2020/all2020content/27/ (accessed on 6 August 2021).

79. Kieffer, H. Advances in the SLIM Lunar Spectral Irradiance Model; Many Observations, One Moon. Available online: https://digitalcommons.usu.edu/calcon/CALCON2021/all2021content/23/ (accessed on 6 December 2021).

80. Coddington, O.M.; Richard, E.C.; Harber, D.; Pilewskie, P.; Woods, T.N.; Chance, K.; Liu, X.; Sun, K. The TSIS-1 Hybrid solar reference spectrum. *Geophys. Res. Lett.* **2021**, *48*, e2020GL091709. [CrossRef]

81. Barreto, A.; Cuevas, E.; Damiri, B.; Guirado, C.; Berkoff, T.; Berjon, A.J.; Hernandez, Y.; Almansa, F.; Gil, M. A new method for nocturnal aerosol measurements with a lunar photometer prototype. *Atmos. Meas. Tech.* **2013**, *6*, 585–598. [CrossRef]

82. Barreto, A.; Cuevas, E.; Granados-Munoz, M.-J.; Alados-Arboledas, L.; Romero, P.M.; Groebner, J.; Kouremeti, N.; Almansa, A.F.; Stone, T.; Toledano, C.; et al. The new sun-sky-lunar Cimel CE318-T multiband photometer—A comprehensive performance evaluation. *Atmos. Meas. Tech.* **2016**, *9*, 631–654. [CrossRef]

83. Umow, V.N. Chromatische depolarisation durch lichtzerstreuung. *Phys. Z.* **1905**, *6*, 674–676.

84. Shkuratov, Y.G.; Opanasenko, N. Is there Umov effect for the Moon in polarization minimum? In Proceedings of the 25th Lunar and Planetary Science Conference, Houston, TX, USA, 14–18 March 1994; p. 1271.

85. Zubko, E.; Videen, G.; Shkuratov, Y.; Muinonen, K.; Yamamoto, T. The Umov effect for single irregularly shaped particles with sizes comparable with wavelength. *Icarus* **2011**, *212*, 403–415. [CrossRef]

86. Gottwald, M.; Bovensmann, H. *SCIAMACHY—Exploring the Changing Earth's Atmosphere*; Springer: Dordrecht, The Netherlands, 2011.

87. Bovensmann, H.; Burrows, J.P.; Buchwitz, M.; Frerick, J.; Noel, S.; Rozanov, V.V.; Chance, K.V.; Goede, A.P.H. SCIAMACHY: Mission objectives and measurement modes. *J. Atmos. Sci.* **1999**, *56*, 127–150. [CrossRef]

88. Frerick, J.; Cozzoni, B.; Slijkhuis, E.; Debeek, R.; Skupin, J. SCIAMACHY In-Flight Calibration. Available online: https://citeseerx.ist.psu.edu/document?repid=rep1&type=pdf&doi=ecb0d75ae276b3e9615d2e40af659744a37cab00 (accessed on 6 December 2021).

89. Liebing, P.; Krijger, M.; Snel, R.; Bramstedt, K.; Noel, S.; Bovensmann, H.; Burrows, J.P. In-flight calibration of SCIAMACHY's polarization sensitivity. *Atmos. Meas. Tech.* **2018**, *11*, 265–289. [CrossRef]

90. Hilbig, T.; Weber, M.; Bramstede, K.; Noel, S.; Burrows, J.P.; Krijger, J.M.; Snel, R.; Meftah, M.; Dame, L.; Bekki, S.; et al. The new SCIAMACHY reference solar spectral irradiance and its validation. *Sol. Phys.* **2018**, *293*, 1–26. [CrossRef]

91. Krijger, J.; Snel, R.; Van Harten, G.; Rietjens, J.; Aben, I. Mirror contamination in space I: Mirror modelling. *Atmos. Meas. Tech.* **2014**, *7*, 3387–3398. [CrossRef]

92. Krijger, M. Development of an Alternative Hyperspectral Moon Phase Reddening Model. Available online: https://www-cdn. eumetsat.int/files/2021-02/ESS-AMM-RP-001-Rev5_LunarModel_FINAL_EUMETSATwebsite.pdf (accessed on 6 December 2021).

93. Urabe, T.; Xiong, X.; Hashiguchi, T.; Ando, S.; Okamura, Y.; Tanaka, K. Radiometric model and inter-comparison results of the SGLI-VNR on-board calibration. *Remote Sens.* **2020**, *12*, 69. [CrossRef]

94. Stone, T.C. Radiometric calibration stability and inter-calibration of solar-band instruments in orbit using the Moon. In Proceedings of the Conference on Earth Observing Systems XIII, San Diego, CA, USA, 11–13 August 2008; pp. 268–276.

95. Eplee, R.E.; Barnes, R.A.; Patt, F.S.; Meister, G.; McClain, C.R. SeaWiFS lunar calibration methodology after six years on orbit. In Proceedings of the Conference on Earth Observing Systems IX, Denver, CO, USA, 2–6 August 2004; pp. 1–13.

96. Choi, T.; Shao, X.; Cao, C. On-orbit radiometric calibration of Suomi NPP VIIRS reflective solar bands using the Moon and solar diffuser. *Appl. Opt.* **2018**, *57*, 9533–9542. [CrossRef]

97. Imai, M.; Kurihara, J.; Kouyama, T.; Kuwahara, T.; Fujita, S.; Sakamoto, Y.; Sato, Y.; Saitoh, S.I.; Hirata, T.; Yamamoto, H.; et al. Radiometric calibration for a multispectral sensor onboard RISESAT microsatellite based on lunar observations. *Sensors* **2021**, *21*, 2429. [CrossRef] [PubMed]

98. Angal, A.; Xiong, X.; Wilson, T. Unscheduled lunar observations for radiometric characterization of VIIRS reflective solar bands. *IEEE Trans. Geosci. Remote Sens.* **2021**, *60*, 1–8. [CrossRef]

99. Tsuchida, S.; Yamamoto, H.; Kouyama, T.; Obata, K.; Sakuma, F.; Tachikawa, T.; Kamei, A.; Arai, K.; Czapla-Myers, J.S.; Biggar, S.F.; et al. Radiometric degradation curves for the ASTER VNIR processing using vicarious and lunar calibrations. *Remote Sens.* **2020**, *12*, 427. [CrossRef]

100. Kouyama, T.; Yokota, Y.; Ishihara, Y.; Nakamura, R.; Yamamoto, S.; Matsunaga, T.; Yamada, M.; Kameda, S.; Sawada, H.; Suzuki, H. Lunar calibration for planetary explorers using SELENE/SP lunar reflectance model. In Proceedings of the 47th Annual Lunar and Planetary Science Conference, Woodlands, TX, USA, 21–25 March 2016; p. 1723.

101. Kouyama, T.; Nakamura, R.; Kato, S.; Kimura, M. Moon observations for small satellite radiometric calibration. In Proceedings of the IEEE International Geoscience & Remote Sensing Symposium, Fort Worth, TX, USA, 23–28 July 2017; pp. 3529–3532.

102. Choi, T.; Shao, X.; Cao, C.; Weng, F. Radiometric stability monitoring of the Suomi NPP Visible Infrared Imaging Radiometer Suite (VIIRS) reflective solar bands using the Moon. *Remote Sens.* **2016**, *8*, 15. [CrossRef]

103. Shao, X.; Cao, C.; Uprety, S.; Padula, F.; Choi, T. Comparing Hyperion lunar observation with model calculations in support of GOES-R Advanced Baseline Imager (ABI) calibration. In Proceedings of the Conference on Earth Observing Systems XIX, San Diego, CA, USA, 18–20 August 2014; pp. 634–642.

104. Taylor, S.; Adriaensen, S.; Toledano, C.; Barreto, Á.; Woolliams, E.; Bouvet, M. LIME: The Lunar Irradiance Model of the European Space Agency. In Proceedings of the EGU General Assembly 2021, Online, 19–30 April 2021; p. EGU21-10066.

105. Neneman, M.; Wagner, S.; Bourg, L.; Blanot, L.; Bouvet, M.; Adriaensen, S.; Nieke, J. Use of Moon observations for characterization of Sentinel-3B Ocean and Land Color Instrument. *Remote Sens.* **2020**, *12*, 2543. [CrossRef]

106. Kieffer, H.H.; Wildey, R.L. Establishing the moon as a spectral radiance standard. *J. Atmos. Ocean. Technol.* **1996**, *13*, 360–375. [CrossRef]

107. Stone, T.C.; Kieffer, H.H. Assessment of uncertainty in ROLO lunar irradiance for on-orbit calibration. In Proceedings of the Conference on Earth Observing Systems IX, Denver, CO, USA, 2–6 August 2004; pp. 300–310.

108. Stone, T.C.; Kieffer, H.; Lukashin, C.; Turpie, K. The Moon as a climate-quality radiometric calibration reference. *Remote Sens.* **2020**, *12*, 1837. [CrossRef]

109. Hayes, D. Stellar absolute fluxes and energy distributions from 0.32 to 4.0 μm. In Proceedings of the Symposium-International Astronomical Union, Tokyo, Japan, 11–15 November 1985; pp. 225–252. [CrossRef]

110. Peterson, D.M.; Hummel, C.A.; Pauls, T.A.; Armstrong, J.T.; Benson, J.A.; Gilbreath, G.C.; Hindsley, R.B.; Hutter, D.J.; Johnston, K.J.; Mozurkewich, D.; et al. Vega is a rapidly rotating star. *Nature* **2006**, *440*, 896–899. [CrossRef]

111. Brown, S.W.; Eplee, R.E., Jr.; Xiong, X. SI-Traceable Top-of-the-Atmosphere lunar irradiance: Potential tie-points to the output of the ROLO model. In Proceedings of the Conference on Earth Observing Systems XXII, San Diego, CA, USA, 6–10 August 2017.

112. Zhang, L.; Zhang, P.; Hu, X.; Chen, L.; Min, M. A novel hyperspectral lunar irradiance model based on ROLO and mean equigonal albedo. *Optik* **2017**, *142*, 657–664. [CrossRef]

113. Lacherade, S.; Aznay, O.; Fougnie, B.; Lebegue, L. POLO: A unique dataset to derive the phase angle dependence of the Moon irradiance. In Proceedings of the Conference on Sensors, Systems, and Next-Generation Satellites XVIII, Amsterdam, The Netherlands, 22–25 September 2014.

114. Lacherade, S.; Viticchiè, B.; Stone, T.; Lebégue, L.; Wagner, S.; Hewison, T. On the phase-angle dependence of the moon calibration results. *GSICS Quat Lunar Calibration* **2013**, *7*, 6–7.

115. Viticchiè, B.; Wagner, S.C.; Hewison, T.J.; Stone, T.C.; Nain, J.; Gutierrez, R.; Müller, J.; Hanson, C. Lunar calibration of MSG/SEVIRI solar channels. In Proceedings of the EUMETSAT Meteorological Satellite Conference, Vienna, Austria, 16–20 September 2013.

116. Barreto, A.; Roman, R.; Cuevas, E.; Berjon, A.J.; Fernando Almansa, A.; Toledano, C.; Gonzalez, R.; Hernandez, Y.; Blarel, L.; Goloub, P.; et al. Assessment of nocturnal aerosol optical depth from lunar photometry at the Izana high mountain observatory. *Atmos. Meas. Tech.* **2017**, *10*, 3007–3019. [CrossRef]

117. Takahashi, M. Lunar data preparation for Himawari-8/-9 AHI. In Proceedings of the 2nd GSICS/CEOS Lunar Calibration Workshop, Xi'an, China, 13–17 November 2017.

118. Velikodsky, Y.I.; Opanasenko, N.V.; Akimov, L.A.; Korokhin, V.V.; Shkuratov, Y.G.; Kaydash, V.G.; Videen, G.; Ehgamberdiev, S.A.; Berdalieva, N.E. New Earth-based absolute photometry of the Moon. *Icarus* **2011**, *214*, 30–45. [CrossRef]

119. Saiki, K.; Saito, K.; Okuno, H.; Suzuki, A.; Yamanoi, Y.; Hirata, N.; Nakamura, R. Estimation of the lunar reflectance by ground-based observation using a tunable liquid-crystal filter telescope. *Earth Planets Space* **2008**, *60*, 417–424. [CrossRef]

120. Shkuratov, Y.; Kaydash, V.; Korokhin, V.; Velikodsky, Y.; Opanasenko, N.; Videen, G. Optical measurements of the Moon as a tool to study its surface. *Planet. Space Sci.* **2011**, *59*, 1326–1371. [CrossRef]

121. Tompkins, S.; Pieters, C.M. Mineralogy of the lunar crust: Results from Clementine. *Meteorit. Planet. Sci.* **1999**, *34*, 25–41. [CrossRef]

122. Yamamoto, S.; Matsunaga, T.; Ogawa, Y.; Nakamura, R.; Yokota, Y.; Ohtake, M.; Haruyama, J.; Morota, T.; Honda, C.; Hiroi, T.; et al. Preflight and in-flight calibration of the spectral profiler on board SELENE (Kaguya). *IEEE Trans. Geosci. Remote Sens.* **2011**, *49*, 4660–4676. [CrossRef]

123. Besse, S.; Yokota, Y.; Boardman, J.; Green, R.; Haruyama, J.; Isaacson, P.; Mall, U.; Matsunaga, T.; Ohtake, M.; Pieters, C. One Moon, many measurements 2: Photometric corrections. *Icarus* **2013**, *226*, 127–139. [CrossRef]

124. Ohtake, M.; Pieters, C.; Isaacson, P.; Besse, S.; Yokota, Y.; Matsunaga, T.; Boardman, J.; Yamomoto, S.; Haruyama, J.; Staid, M. One Moon, many measurements 3: Spectral reflectance. *Icarus* **2013**, *226*, 364–374. [CrossRef]

125. Walther, A.; Heidinger, A.K.; Miller, S. The expected performance of cloud optical and microphysical properties derived from Suomi NPP VIIRS Day/Night Band lunar reflectance. *J. Geophys. Res. Atmos.* **2013**, *118*, 13230–13240. [CrossRef]

126. Hu, S.; Ma, S.; Yan, W.; Jiang, J.; Huang, Y. A new multichannel threshold algorithm based on radiative transfer characteristics for detecting fog/low stratus using night-time NPP/VIIRS data. *Int. J. Remote Sens.* **2017**, *38*, 5919–5933. [CrossRef]

127. Kieffer, H.H.; Anderson, J.M. Use of the Moon for spacecraft calibration over 350–2500 nm. In Proceedings of the Conference on Sensors, Systems, and Next-Generation Satellites II, Barcelona, Spain, 21–24 September 1998; pp. 325–336.

128. Sindy, S.; Stefan, A. PROBA-V Vicarious Calibration: Investigation into the Impact of In-Orbit Temperature Variation. Available online: http://gsics.atmos.umd.edu/pub/Development/20210812/PROBAV_calibration_GSICS_aug2021.pdf (accessed on 12 December 2021).

129. Kieffer, H. Status of the SLIMED lunar model. *GSICS Quat* **2022**, *15*, 7–9.

130. Cao, C.; Bai, Y.; Wang, W.; Choi, T. Radiometric inter-consistency of VIIRS DNB on Suomi NPP and NOAA-20 from observations of reflected lunar lights over deep convective clouds. *Remote Sens.* **2019**, *11*, 934. [CrossRef]

131. Xi, S.; Changyong, C.; Sirish, U. Comparing Hyperion-Observed with Model-Predicted Lunar Irradiances in Support of GOES-R ABI Calibration. Available online: https://digitalcommons.usu.edu/calcon/CALCON2012/All2012Content/55/ (accessed on 12 December 2019).

132. Kieffer, H.H.; Jarecke, P.; Pearlman, J. Initial lunar calibration observations by the EO-1 Hyperion imaging spectrometer. In Proceedings of the International Symposium on Optical Science and Technology, San Diego, CA, USA, 29 July–3 August 2002; pp. 247–258.

133. Xiong, X.; Sun, J.; Fulbright, J.; Wang, Z.; Butler, J.J. Lunar calibration and performance for S-NPP VIIRS reflective solar bands. *IEEE Trans. Geosci. Remote Sens.* **2016**, *54*, 1052–1061. [CrossRef]

134. Meygret, A.; Blanchet, G.; Colzy, S.; Gross-Colzy, L. Improving ROLO lunar albedo model using PLEIADES-HR satellites extra-terrestrial observations. In Proceedings of the Conference on Earth Observing Systems XXII, San Diego, CA, USA, 6–10 August 2017.

135. Mishra, N.; Haque, M.O.; Leigh, L.; Aaron, D.; Helder, D.; Markham, B. Radiometric cross calibration of Landsat 8 Operational Land Imager (OLI) and Landsat 7 Enhanced Thematic Mapper Plus (ETM plus). *Remote Sens.* **2014**, *6*, 12619–12638. [CrossRef]

136. Xiong, X.; Angal, A.; Twedt, K.A.; Chen, H.; Link, D.; Geng, X.; Aldoretta, E.; Mu, Q. MODIS reflective solar bands on-orbit calibration and performance. *IEEE Trans. Geosci. Remote Sens.* **2019**, *57*, 6355–6371. [CrossRef]

137. Chen, L.; Zhang, P.; Wu, R.; Hu, X.; Zhang, L. Monitoring radiometric response change of visible band for FY-2 geostationary meteorological satellite by lunar target. *J. Remote Sens.* **2018**, *22*, 211–219. (In Chinese)

138. Wu, R.; Zhang, P.; Yang, Z.; Hu, X.; Ding, L.; Chen, L. Monitor radiance calibration of the remote sensing instrument with reflected lunar irradiance. *J. Remote Sens.* **2016**, *20*, 278–289. (In Chinese)

139. Sun, J.; Xiong, X. Improved lunar irradiance model using multiyear MODIS lunar observations. *IEEE Trans. Geosci. Remote Sens.* **2021**, *59*, 5154–5170. [CrossRef]

140. Roman, R.; Gonzalez, R.; Toledano, C.; Barreto, A.; Perez-Ramirez, D.; Benavent-Oltra, J.A.; Olmo, F.J.; Cachorro, V.E.; Alados-Arboledas, L.; de Frutos, A.M. Correction of a lunar-irradiance model for aerosol optical depth retrieval and comparison with a star photometer. *Atmos. Meas. Tech.* **2020**, *13*, 6293–6310. [CrossRef]

141. Zhang, L.; Zhang, P.; Hu, X.; Chen, L.; Min, M.; Xu, N.; Wu, R. Radiometric cross-calibration for multiple sensors with the Moon as an intermediate reference. *J. Meteorol. Res.* **2019**, *33*, 925–933. [CrossRef]

142. Cao, C.; Vermote, E.; Xiong, X. Using AVHRR lunar observations for NDVI long-term climate change detection. *J. Geophys. Res. Atmos.* **2009**, *114*, D20105. [CrossRef]

143. Shao, X.; Choi, T.; Cao, C.; Blonski, S.; Wang, W.; Bai, Y. Trending of Suomi-NPP VIIRS radiometric performance with lunar band ratio. In Proceedings of the Conference on Earth Observing Missions and Sensors—Development, Implementation, and Characterization III, Beijing, China, 13–15 October 2014.

144. Bali, M.; Ferraro, R.R.; Zou, C.Z.; Hewison, T.; Flynn, L.E.; Doelling, D.R. GSICS references for monitoring geostationary and polar instruments. In *AGU Fall Meeting Abstracts*; American Geophysical Union: Washington, DC, USA, 2018; p. A24B-07.

145. Cramer, C.E.; Lykke, K.R.; Woodward, J.T.; Smith, A.W. Precise measurement of lunar spectral irradiance at visible wavelengths. *J. Res. Natl. Inst. Stand. Technol.* **2013**, *118*, 396–402. [CrossRef]

146. Wagner, S.; Mattioli, V.; Stone, T.; Hu, X.; Wu, X. Outcome of the Third Joint GSICS/IVOS Lunar Calibration Workshop. Available online: https://repository.library.noaa.gov/view/noaa/29005/noaa_29005_DS1.pdf (accessed on 6 October 2020).

147. Stone, T.C. Addressing Needs to Achieve High-Accuracy Lunar Calibration. Available online: https://digitalcommons.usu.edu/calcon/CALCON2022/All2022Content/5/ (accessed on 6 January 2023).

148. Cataford, A.; Gadsden, S.A.; Turpie, K. Air-LUSI: Autonomous telescope design for lunar spectral irradiance measurements. In Proceedings of the Conference on Advanced Optics for Imaging Applications—UV through LWIR IV, Baltimore, MD, USA, 14–15 April 2019.

149. Newton, A.; Maxwell, S.E.; Gadsden, S.A.; Turpie, K. Air-LUSI: Performance analysis of a high-altitude robotic telescope used for tracking the Moon. In Proceedings of the 2020 Canadian Society for Mechanical Engineering International Congress, Charlottetown, PE, Canada, 21–24 June 2020; pp. 21–24.

150. Turpie, K.; Brown, S.; Woodward, J.; Gadsden, A.; Stone, T.; Grantham, S.; Maxwell, S.; Larason, T.; Newton, A.; Rice, J. Airborne Lunar Spectral Irradiance (Air-LUSI) Mission Capability Demonstration. Available online: https://digitalcommons.usu.edu/calcon/CALCON2020/all2020content/25/ (accessed on 6 February 2021).

151. Woodward, J.T.; Turpie, K.; Stone, T.; Gadsden, S.; Newton, A.; Maxwell, S.; Grantham, S.; Larason, T.; Brown, S. Measurements of absolute, SI-traceable lunar irradiance with the airborne lunar spectral irradiance (air-LUSI) instrument. *Metrologia* **2022**, *59*, 034001. [CrossRef]

152. Stone, T.C.; Turpie, K.; Brown, S.; Maxwell, S.; Woodward, J. Evaluation of Air-LUSI Measurements to Advance Lunar Modeling and the ROLO Lunar Calibration Reference. Available online: https://digitalcommons.usu.edu/calcon/CALCON2020/all2020content/25/ (accessed on 18 December 2021).

153. Kopp, G.; Smith, P.; Belting, C.; Castleman, Z.; Drake, G.; Espejo, J.; Heuerman, K.; Lanzi, J.; Stuchlik, D. Radiometric flight results from the HyperSpectral Imager for Climate Science (HySICS). *Geosci. Instrum. Meth.* **2017**, *6*, 169–191. [CrossRef]

154. Lukashin, C.; Jackson, T.; Cooney, M.; Ryan, N.; Beverly, J.; Young, C.; Rutherford, G.; Davis, W.; Nguyen, T.; Swanson, R.; et al. ARCSTONE: Calibration of Lunar Spectral Reflectance. Available online: https://digitalcommons.usu.edu/calcon/CALCON2018/all2018content/24/ (accessed on 10 February 2020).

155. Lukashin, C.; Stone, T.; Kopp, G.; Jackson, T.; Swanson, R.; Abraham, N.; Minda, E.; Buleri, C.; Carvo, J.; Cooney, M.; et al. ARCSTONE: Calibration of Lunar Spectral Reflectance from Space. Available online: https://digitalcommons.usu.edu/calcon/CALCON2019/all2019content/9/ (accessed on 3 January 2020).

156. Lukashin, C.; Kopp, G.; Jackson, T.; Swanson, R.; Buleri, C.; Young, C.; Gorman, M.; Zeigler, M.; Stone, T. ARCSTONE: Calibration of Lunar Spectral Reflectance from Space ESTO InVEST (Update). Available online: https://digitalcommons.usu.edu/calcon/CALCON2022/All2022Content/4/ (accessed on 6 January 2023).

157. Swanson, R.; Kehoe, M.; Stebbins, M.; Courrier, H.; Lukashin, C.; Jackson, T.; Cooney, M.; Davis, W.; Kopp, G.; Smith, P.; et al. The ARCSTONE project to calibrate lunar reflectance. In Proceedings of the 2020 IEEE Aerospace Conference, Big Sky, MT, USA, 7–14 March 2020; pp. 1–10.

158. Wang, Y.; Huang, Y.; Wang, S.; Li, Z.; Zhang, Z.; Hu, X.; Zhang, P. Ground-based observation system development for the Moon hyper-spectral imaging. *Publ. Astron. Soc. Pac.* **2017**, *129*, 055002. [CrossRef]

159. Berk, A.; Conforti, P.; Kennett, R.; Perkins, T.; Hawes, F.; Van Den Bosch, J. MODTRAN®6: A major upgrade of the MODTRAN®radiative transfer code. In Proceedings of the 2014 6th Workshop on Hyperspectral Image and Signal Processing: Evolution in Remote Sensing (WHISPERS), Lausanne, Switzerland, 24–27 June 2014; pp. 1–4.

160. Wang, Y.; Hu, X.; Chen, L.; Huang, Y.; Li, Z.; Wang, S.; Zhang, P.; Wu, R.; Zhang, L.; Wang, W. Comparison of the lunar models using the hyper-spectral imager observations in Lijiang, China. *Remote Sens.* **2020**, *12*, 1878. [CrossRef]

161. Hewison, T.J.; Doelling, D.R.; Lukashin, C.; Tobin, D.; John, V.O.; Joro, S.; Bojkov, B. Extending the Global Space-based Inter-Calibration System (GSICS) to tie satellite radiances to an absolute scale. *Remote Sens.* **2020**, *12*, 1782. [CrossRef]

162. Zhang, P.; Lu, N.; Li, C.; Ding, L.; Zheng, X.; Zhang, X.; Hu, X.; Ye, X.; Ma, L.; Xu, N.; et al. Development of the Chinese space-based radiometric benchmark mission LIBRA. *Remote Sens.* **2020**, *12*, 2179. [CrossRef]

163. Wielicki, B.A.; Young, D.F.; Mlynczak, M.G.; Thome, K.J.; Leroy, S.; Corliss, J.; Anderson, J.G.; Ao, C.O.; Bantges, R.; Best, F.; et al. Achieving climate change absolute accuracy in orbit. *Bull. Am. Meteorol. Soc.* **2013**, *94*, 1519–1539. [CrossRef]

164. Leckey, J. Climate Absolute Radiance and Refractivity Observatory (CLARREO). In Proceedings of the 36th International Symposium on Remote Sensing of the Environment (ISRSE), Berlin, Germany, 11–15 May 2015; pp. 213–217.

165. Fox, N.; Green, P.; Brindley, H.; Russell, J.; Smith, D.; Lobb, D.; Cutter, M.; Barnes, A. TRUTHS (Traceable Radiometry Underpinning Terrestrial and Helio Studies): A mission to achieve climate quality data. In Proceedings of the ESA Living Planet Symposium 2013, Edinburgh, UK, 9–13 September 2013.

166. Shea, Y.L.; Baize, R.; Fleming, G.; Johnson, D.; Lukashin, C.; Mlynczak, M.; Thome, K.; Wielicki, B. Climate Absolute Radiance and Refractivity Observatory (CLARREO) Pathfinder Mission: Status Overview. Available online: https://digitalcommons.usu.edu/calcon/CALCON2016/all2016content/3/ (accessed on 11 April 2020).

167. Shea, Y.; Fleming, G.; Kopp, G.; Lukashin, C.; Pilewskie, P.; Smith, P.; Thome, K.; Wielicki, B.; Liu, X.; Wu, W.; et al. CLARREO Pathfinder: Mission overview and current status. In Proceedings of the IEEE International Geoscience and Remote Sensing Symposium (IGARSS), Online, 26 September–2 October 2020; pp. 3286–3289.

168. Stone, T.C.; Lukashin, C.; Kopp, G. Calibration Acquisitions of the Moon by CLARREO Pathfinder. Available online: https://digitalcommons.usu.edu/calcon/CALCON2016/all2016content/3/ (accessed on 15 November 2019).

169. NASA. NASA CLARREO Pathfinder Web Page. Available online: https://clarreo-pathfinder.larc.nasa.gov/gallery/clarreo-pathfinder-iss-inter-calibration-with-sun-and-moon/# (accessed on 1 January 2021).

170. NASA. Mission Overview. Available online: https://clarreo-pathfinder.larc.nasa.gov/mission-overview/#project-timeline (accessed on 10 January 2020).

171. Fox, N.; Green, P. Traceable Radiometry Underpinning Terrestrial- and Helio-Studies (TRUTHS): An element of a space-based climate and calibration observatory. *Remote Sens.* **2020**, *12*, 2400. [CrossRef]

172. Fox, N.; Shea, Y.; Fehr, T.; Gary, F.; Lukashin, C.; Pilewskie, P.; Remedios, J.; Smith, P. Toward a climate and calibration observatory in space: NASA CLARREO Pathfinder and ESA TRUTHS. In Proceedings of the 23rd EGU General Assembly Conference, Online, 19–30 April 2021; p. EGU21-14656.

173. Fox, N.; Green, P.; Gorron, J. Traceable Radiometry Underpinning Terrestrial- and Helio-Studies (TRUTHS): Enabling a Space-Based Climate and Calibration Observatory—An ESA Earth Watch Mission. Available online: http://newrad2021.aalto.fi/docs/EAO/EAO_OR_012.pdf (accessed on 7 December 2021).

174. ESA. TRUTHS: A Standards Laboratory in Space. Available online: https://www.esa.int/ESA_Multimedia/Images/2021/10/TRUTHS_a_standards_laboratory_in_space (accessed on 1 January 2021).

175. Lu, N.; Ding, L.; Zheng, X.; Ye, X.; Li, C.; Lyu, D.; Zhang, P.; Hu, X.; Zhou, C.; You, Z.; et al. Introduction of the radiometric benchmark satellite being developed in China for remote sensing. *J. Remote Sens.* **2020**, *24*, 672–680. (In Chinese)

176. Wang, Y.; Hu, X.; Wang, H.; Ye, X.; Fang, W. Standard transfer chain for radiometric calibration of optical sensing instruments with traceability in solar reflective bands. *Opt. Precis. Eng.* **2015**, *23*, 1807–1812. (In Chinese) [CrossRef]

177. Korokhin, V.; Velikodsky, Y.I.; Shkuratov, Y.G.; Mall, U. The phase dependence of brightness and color of the lunar surface: A study based on integral photometric data. *Sol. Syst. Res.* **2007**, *41*, 19–27. [CrossRef]

178. Kaydash, V.; Pieters, C.; Shkuratov, Y.; Korokhin, V. Lunar opposition effect as inferred from Chandrayaan-1 M3 data. *J. Geophys. Res. Planets* **2013**, *118*, 1221–1232. [CrossRef]

179. Berezhnoi, A.; Velikodsky, Y.I.; Pakhomov, Y.V.; Wöhler, C. The surface of the Moon as a calibration source for Na and K observations of the lunar exosphere. *Planet. Space Sci.* **2023**, *228*, 105648. [CrossRef]

180. Hapke, B. *Theory of Reflectance and Emittance Spectroscopy*; Cambridge University Press: Cambridge, UK, 2012.